



Ice-supersaturated air masses in the northern mid-latitudes from regular in-situ observations by passenger aircraft: vertical distribution, seasonality and tropospheric fingerprint

Andreas Petzold¹, Patrick Neis^{1,3,§}, Mihai Rütimann¹, Susanne Rohs¹, Florian Berkes^{1,§},
 5 Herman G.J. Smit¹, Martina Krämer^{2,3}, Nicole Spelten², Peter Spichtinger³, Philippe Nedelec⁴,
 and Andreas Wahner¹,

¹Forschungszentrum Jülich GmbH, Institute of Energy and Climate Research 8 – Troposphere, Jülich, Germany

²Forschungszentrum Jülich GmbH, Institute of Energy and Climate Research 7 – Stratosphere, Jülich, Germany

³Johannes Gutenberg University, Institute for Atmospheric Physics, Mainz, Germany

10 ⁴CNRS Laboratoire d'Aérodynamique, and Université Paul Sabatier Toulouse III, Toulouse, France

[§] now at CGI Deutschland B.V. & CO. KG, Frankfurt, Germany

[§] now at P3 solutions GmbH, Aachen, Germany

Correspondence to: Andreas Petzold (a.petzold@fz-juelich.de)

Abstract. The vertical distribution and seasonal variation of upper tropospheric humidity (UTH) and particularly
 15 of ice-supersaturated air masses in the extratropical upper troposphere and lowermost stratosphere (Ex-UTLS) is
 investigated at northern mid-latitudes over the regions Eastern North America, the North Atlantic and Europe for
 the period 1995 to 2010. Observation data originate from regular and continuous long-term measurements of
 water vapour volume mixing ratio (H_2O VMR), temperature and relative humidity with respect to ice (RH_{ice}) by
 instrumented passenger aircraft in the framework of the European research program MOZAIC (1994 – 2010)
 20 which is continued as European research infrastructure IAGOS (from 2011). The in-situ observations of UTH
 with a vertical resolution of 30 hPa (< 800 m at tropopause level) and a horizontal resolution of 1 km resolve
 detailed features of the distribution of water vapour and ice-supersaturated air relative to the thermal tropopause,
 including their seasonal and regional variability and chemical signatures at various distances from the tropopause
 layer. Annual cycles of the vertical distribution of UTH over the investigated regions demonstrate annually
 25 increasing H_2O VMR above the thermal tropopause in the summer months, but without an associated increase in
 RH_{ice} . Over all investigated regions, upper tropospheric air masses close to the tropopause level are nearly
 saturated with respect to ice and contain a significant fraction of ice-supersaturated regions (ISSR) with a distinct
 seasonal cycle of minimum values in summer (30% over the ocean, 20 - 25% over land), and maximum values in
 late winter (35 - 40% over both land and ocean). Above the thermal tropopause, ISSR are occasionally observed
 30 with an occurrence probability of $1.5 \pm 1.1\%$, whereas above the dynamical tropopause at 2 PVU, the occurrence
 probability increases 4-fold to $8.4 \pm 4.4\%$. In both tropopause-height (TPH) related coordinate systems, the ISSR
 occurrence probabilities drop to values below 1% for the next higher air mass layer with pressure levels $p < p_{TPH}$
 – 15 hPa. For both tropopause definitions, the tropospheric nature or fingerprint, respectively, based on O_3 VMR,
 indicate continuing dominant tropospheric influence on ISSR inside and above the respective tropopause layer.
 35 For the non-ISSR, however, the stratospheric nature is clearly visible above the thermal tropopause whereas



above the dynamical tropopause the air masses show still a relevant tropospheric influence. For all three regions, seasonal deviations from the long-term annual cycle of ISSR occurrence show no significant trends over the observation period of 15 years, whereas weak but significant dependencies of ISSR occurrence on the North Atlantic Oscillation (NAO) index are observed.

40 1 Introduction

Upper tropospheric humidity (UTH) and in particular ice-supersaturated air masses ($RH_{ice} > 100\%$) are of ample importance for the occurrence and life cycle of high ice clouds, or cirrus clouds, respectively, which have a large but still not fully understood impact on Earth's climate, with its net radiation impact being unknown and even the sign being unclear (Chen et al., 2000; Boucher et al., 2013). In this context, long-term observations of UTH
45 are an indispensable prerequisite for the investigation of potential changes of water vapour abundance in the global UTLS (e.g., Müller et al., 2016), and the resulting effects on atmospheric radiation (e.g., Riese et al., 2012) and on cirrus cloud occurrence and life cycle (Gettelman et al., 2012; Krämer et al., 2016; Heymsfield et al., 2017).

The vertical distribution of water vapour around the tropopause is characterized by a steep decrease of H_2O
50 volume mixing ratio (VMR) up to the thermal tropopause. Across the tropopause layer, H_2O VMR decreases further but less steep until it reaches its near-constant stratospheric value at about 2 km altitude above the tropopause layer. The thermal tropopause forms thus an efficient barrier for the vertical transport of H_2O into the stratosphere, whereas troposphere-stratosphere transport occurs for specific local-scale dynamic situations such as, e.g., tropopause folds (Hoor et al., 2004; Gettelman et al., 2011).

55 These features are reported from extensive research campaigns like SPURT (Hoor et al., 2004) which was designed on a climatological approach and compared to climatological data from the research programme MOZAIC (Marenco et al., 1998), and from long-term sampling by the CARIBIC passenger aircraft which carries an instrumented airfreight container (Dyroff et al., 2014; Zahn et al., 2014), or by instrumented balloons (Kunz et al., 2013). The complex structure of the Ex-UTLS, and the extratropical transition layer are described in-depth
60 in the review article by Gettelman et al. (2011).

Of particular interest with respect to UTH and ice cloud formation and life cycle is the thermodynamic state parameter RH_{ice} which controls the properties of ice clouds by setting the thermodynamic conditions for cirrus cloud formation, existence and dissolution (Pruppacher and Klett, 1997). Air masses supersaturated with respect to ice ($RH_{ice} > 100\%$), so called ice-supersaturated regions (ISSR), have faced a decrease in temperature,
65 increase in pressure, or increase in water vapour mixing ratio, i.e. specific humidity during their past lifetime (Spichtinger and Leschner, 2016). As a result, these air parcels are both colder and more humid than the embedding sub-saturated atmosphere (Gierens et al., 1999; Spichtinger et al., 2003b) which did not experience similar changes in their atmospheric state parameters.

In the northern mid-latitudes, ISSR occurrence coincides strongly with the storm tracks over the North Atlantic
70 (Spichtinger et al., 2003b; Gettelman et al., 2006; Lamquin et al., 2012). Frequently occurring synoptic weather features such as fronts or warm conveyor belts lead to synoptic-scale upward motion and thus facilitate the formation of ISSR (Spichtinger et al., 2005). However, ice-supersaturation, occurs as well in regions of high pressure and anticyclonic flow (Gierens and Brinkop, 2012). Detailed studies of the ISSR life cycle by means of Lagrangian trajectory analyses (Irvine et al., 2014) indicate that the lifetime of an air parcel in the state of



75 supersaturation below the tropopause is generally short with the median duration being less than 6 hours for both winter and summer conditions. In an Eulerian view, however, these ISSR regions as composed of many supersaturated air parcels may persist on a much longer time scale (Spichtinger et al., 2005).

In contrast to the strong negative gradient in H_2O VMR at altitudes below but close to the tropopause, ISSR occur frequently in the humid and cold upper tropospheric air masses close to the thermal tropopause. Detailed
80 investigations of the distribution and structure of ice-supersaturation in the northern mid-latitude tropopause region over Lindenberg, Germany, from 15 months of balloon soundings showed that ice saturation occurs in most cases below the tropopause, even in meteorological situations where the tropopause pressure is relatively high (Spichtinger et al., 2003a). On the other hand, the occurrence of ISSR above the thermal tropopause is very rare with a fraction of approx. 6% of the observations over Lindenberg, reporting ice-supersaturation above the
85 thermal tropopause. Direct evidence of the occurrence of ice-supersaturation above but close to the thermal tropopause report a fraction of 2% from an earlier analysis of MOZAIC data (Gierens et al., 1999).

ISSR constitute potential formation regions for ice clouds, persistent contrails and contrail-cirrus. In these cold and humid air masses, natural cirrus clouds may form by heterogeneous or homogeneous freezing processes (Koop et al., 2000; Hoose and Möhler, 2012; Heymsfield et al., 2017), and long-lived contrails and contrail-
90 cirrus are generated by cruising aircraft, causing the major non- CO_2 climate impact of civil aviation (Aaltonen et al., 2006; Stuber et al., 2006; Burkhardt et al., 2008; Lee et al., 2010; Burkhardt and Kärcher, 2011; Kärcher, 2018; Bock and Burkhardt, 2019).

The occurrence of ISSR and its close link to the occurrence of cirrus clouds is reported from a joint analysis of SAGE II data on subvisible cirrus and MOZAIC ice-supersaturation by Gierens et al. (2000) which provides an
95 almost 1:1 relationship between subvisible cirrus occurrence and ice-supersaturation, but without discrimination between tropospheric and stratospheric air masses. From other platforms, there are only very few reports of cirrus clouds above the tropopause layer, either from satellite retrievals (Spang et al., 2015) or from research aircraft flights (Müller et al., 2015).

Despite the high climate-related relevance of the vertical distribution of water vapour VMR and related RH_{ice} in
100 the vicinity of the extratropical tropopause layer, there exist only very few approaches for the continuous global-scale monitoring of water vapour abundance and UTH with sufficient precision and vertical resolution; see Müller et al. (2016) for an overview. Among space-borne techniques, the High-Resolution Infrared Radiation Sounder (HIRS) instruments are most important since they cover more than 3 decades of observations (Gierens et al., 2014), whereas the Microwave Limb Sounder (MLS) and the Atmospheric InfraRed Sounder (AIRS) were
105 particularly used for the space-borne global mapping of ISSR (Spichtinger et al., 2003b; Lamquin et al., 2012) and cirrus cloud coverage (Stubenrauch et al., 2010). However, the vertical resolution provided by space-borne instruments in the Ex-UTLS is very limited and does not allow detailed studies on the vertical distribution of UTH in this region.

Concerning in-situ observations of water vapour, the international radiosonde network is in operation for many
110 decades but the observations are considered insufficient for detecting trends and variability in UTLS water vapour (Seidel et al., 2009).

The only other existing global-scale in-situ observation infrastructure for atmospheric composition in the Ex-UTLS uses instrumented passenger aircraft for routine measurements of trace gases, aerosols and clouds at cruise altitude. IAGOS (In-service Aircraft for a Global Observing System; see Petzold et al. (2015), Nédélec et al. (2015), and www.iagos.org for details) and its predecessor research programs MOZAIC (Marengo et al.,
115 al. (2015), and www.iagos.org for details) and its predecessor research programs MOZAIC (Marengo et al.,

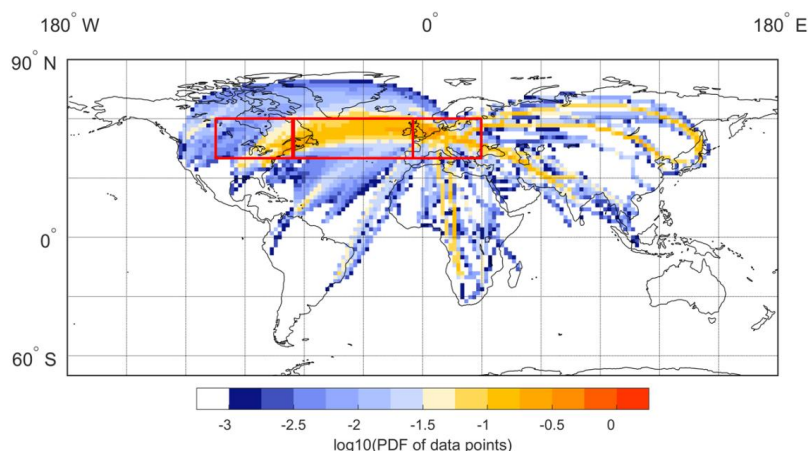


1998) and CARIBIC (Brenninkmeijer et al., 1999; Brenninkmeijer et al., 2007) conduct regular measurements of UTH since 1994. The transformation of both former research projects MOAZIC and CARIBIC into the current IAGOS Research Infrastructure took place in 2011. These regular flights on a global scale are unique in its quantity, continuity, and quality of measurements of Ex-UTLS air masses and have provided detailed insights into the distribution of RH_{ice} (Gierens et al., 1999; Spichtinger et al., 2002), the distribution and properties of ISSR (Gierens and Spichtinger, 2000; Spichtinger and Leschner, 2016), their link to cirrus clouds (Gierens et al., 2000; Petzold et al., 2017), and the processes controlling the water vapour distribution (Zahn et al., 2014). In the present study, we analysed the distribution properties of RH_{ice} and of ISSR in the Ex-UTLS for a latitudinal band reaching from Eastern North America across the North Atlantic to Europe. We used the full MOZAIC period from 1995 to 2010 which permits the robust seasonal analysis for the identified target regions. Our studies focus on the structure of the vertical distribution of RH_{ice} , its variability and seasonality, and potential trends. The vertical resolution of our data is set to 30 hPa, which corresponds to a vertical distance of approx. 800 m at 10 km altitude for U.S. Standard Atmosphere conditions (NASA, 1976), and is of similar order as the typical resolution of UTLS models. General circulation models of the middle atmosphere like L90MA and L47MA use a vertical grid spacing of 10 – 20 hPa near the extratropical tropopause (Jöckel et al., 2016) which is reflected in the selected vertical resolution of MOZAIC data layers.

2 MOZAIC RH data set

2.1 Data coverage and vertical distribution

The MOZAIC RH data set used for this analysis spans over the period from 1995 to 2010 and is constrained to cruise altitude conditions, i.e., pressure below 350 hPa (above approx. 8 km altitude), and to ambient temperatures below 233 K to exclude potential sensor contamination by supercooled liquid water droplets. The areal boundaries of the analysed data set are 40 °N to 60 °N and cover the regions Eastern North America (105 °W to 65 °W), North Atlantic (65 °W to 5 °W) and Europe (5 °W to 30 °E). Figure 1 illustrates the global coverage of water vapour observations by MOZAIC for years 1995 to 2010. Inserted boxes mark the regions Eastern North America, North Atlantic and Europe. The annual data coverage for all analysed regions varies between 30 hours and 65 hours of flight per season (3 months) which corresponds to 27,000 to 60,000 data points of 4 s duration each, per season per year. All investigated regions are characterized by continuous data coverage over the investigated period with no data gaps. Data are available to open access through the IAGOS data portal at www.iagos.org. Since MOZAIC data are collected at constant-pressure cruise levels of passenger aircraft which may cross from the upper troposphere (UT) through the tropopause layer (TPL) into the lowermost stratosphere (LMS) and back, the data vertical coordinates are reported relative to the tropopause pressure level. The extratropical tropopause layer height can be defined following different criteria (Ivanova, 2013). The thermal tropopause according to WMO criteria (WMO, 1957) is defined as the level, where the lapse-rate decreases to 2 K km⁻¹ or less and remains so small at least in the overlying layer of 2 km. This definition, however, allows for the existence of multiple tropopause layers. The dynamical definition of the tropopause is based on the potential vorticity with 1 PVU = 10⁻⁶ m² Ks⁻¹ kg⁻¹. The values of the potential vorticity in the stratosphere exceed its values in the troposphere by an order of magnitude. The threshold value of 2 PVU for separating tropospheric and



155

Figure 1. Global coverage of water vapour observations by MOZAIC for the period 1995 to 2010, shown as decadal logarithm of the probability distribution function (PDF) of the data points; red boxes indicate the target areas for our analyses.

160 stratospheric air masses is commonly used in studies on stratosphere–troposphere transport (Gettelman et al., 2011; Ivanova, 2013). The bulk of our analyses refer to the classic thermal tropopause according to WMO criteria (WMO, 1957), with the exception of the occurrence of ISSR above the tropopause, where we present the analyses for both tropopause definitions and compare the results; see Section 3.3. The pressure levels of the thermal tropopause (p_{TPHWMO}) and the dynamical 2 PVU tropopause (p_{TPHDYN}) are derived from ERA-Interim data (Dee et al., 2011). They are used to determine the position of the aircraft relative to this layer and thus to distinguish whether the aircraft sampled air masses of UT, TPL or LMS origin.

165

The separation is achieved by applying the following criteria (formulated for the thermal tropopause only):

LMS : $p < p_{\text{TPHWMO}} - 15\text{hPa}$; which is limited by the maximum cruise altitude with $p \approx 190\text{ hPa}$;

TPL : $p = p_{\text{TPHWMO}} \pm 15\text{hPa}$;

170

UT : $p > p_{\text{TPHWMO}} + 15\text{hPa}$; limited to lower altitudes by $p < 350\text{hPa}$.

In order to reach both a sufficiently large data set for robust statistical analyses and good vertical resolution, the Ex-UTLS is subdivided into 7 layers of 30 hPa thickness each, with three layers below the TPL and 3 layers above. Thouret et al. (2006) used a similar definition, but referenced to the dynamical tropopause at 2 PVU. A more detailed description of the methodology for determining the aircraft position relative to the thermal tropopause and for the vertical resolution of the data set is given by Berkes et al. (2017). Since each data set from one single flight provides only a one-dimensional snapshot of the state of the atmosphere along the flight track, and each aircraft cruises at a slightly different pressure level, data are consolidated to 3-months season files, allowing the analysis of vertical distributions of atmospheric state parameters on a robust statistical basis.

175

2.2 RH instrumentation

180 The relative humidity measurements of MOZAIC and today IAGOS use a thin-film capacitive sensor of type Humicap (Vaisala) which is mounted inside an aeronautic Rosemount inlet to the aircraft skin. The MOZAIC Capacitive Hygrometers (MCH) are calibrated in the laboratory against a Lyman α resonance fluorescence



hygrometer (Kley and Stone, 1978) with respect to RH over liquid water (Helten et al., 1998; Smit et al., 2014). The conversion to RH_{ice} uses the equations by Sonntag (1994). The MCH reports RH data with an uncertainty of
185 4% RH in the middle troposphere and 6% RH at the tropopause (Smit et al., 2014). The deployed sensor has been carefully compared to high-precision water vapour instruments in dedicated research aircraft studies (Helten et al., 1999; Neis et al., 2015a; Neis et al., 2015b) which demonstrate a remarkably good agreement between the MCH and reference instruments with $R^2 = 0.92$ and a slope of $m = 1.02$ from linear regression analyses. The authors report an MCH uncertainty of 5% RH which is in close agreement with the uncertainty
190 determined from error propagation analysis (Smit et al., 2014).

Applying the 2- σ criterion (95% confidence level), the MCH limit of detection (LOD) is $RH_{ice,LOD} = 12\%$ which transfers into a minimum detectable H_2O VMR of approx. 10 ppmv at typical mid-latitude upper troposphere conditions ($T = 218K$, $p = 250$ hPa). Kunz et al. (2008) who performed a statistical analysis of water vapour measurements from the SPURT campaigns between 2001 and 2003 by a Lyman- α photo-fragment fluorescence
195 hygrometer (Zöger et al., 1999; Meyer et al., 2015) and MOZAIC water vapour data from the same period applied a similar LOD value of 10 ppmv.

2.3 RH data processing

The processing of the MCH data had been subject to a calibration error from year 2000 on. This error in the data analysis caused a bias of data towards higher RH_{ice} values and shifted the peak value of the RH_{ice} probability
200 distribution function (PDF) for in-cloud observations to approx. 130% RH_{ice} which is far above the physically expected value of 100% RH_{ice} . Earlier MCH data for the period 1995 to 1999, however, are not affected. The publications by Lamquin et al. (2012) (Fig. 5 of that publication) and Penner et al. (2018) (Fig. 6 of that publication) illustrate the shift of the erroneous MOZAIC data towards higher RH_{ice} values very clearly.

The calibration error was corrected in a recent reanalysis and the PDFs of RH_{ice} are now consistent for the full
205 MOZAIC period and physically reasonable with the PDF showing a second maximum at 100% RH_{ice} , as expected for in-cloud sequences (Smit et al., 2014).

Besides the calibration error, another limitation of the MOZAIC RH data set stemming from MCH sensor drifts, required correction. In its standard operation mode, MCH sensors were replaced every 3 to 6 months. During their deployment periods, the sensors showed occasionally drifts of the sensor output signal caused by a shift of
210 the sensor offset voltage, which results in erroneously high RH_{ice} values. To overcome this measurement artefact, the so-called in-flight calibration method (IFC) was developed by Smit et al. (2008), which references the offset voltage of the sensor to signals from flight sequences in dry stratospheric air masses where the expected RH_{ice} signal is below the MCH LOD and thus the true MCH signal is considered zero RH.

The methodology is illustrated in Figure 2: The MCH sensors leave the calibration facility with a baseline for
215 dry conditions (green curve); the theoretical signal expected from the stratospheric H_2O background of 5 ppmv is then added and this new baseline (blue curve) is the reference line for the offset determination. In the operational mode of the IFC method, the lower bound values of the MCH signal during an operational period of typically 15 consecutive flights are determined as the observations below the 1 Percentile value (P01) of the data collected

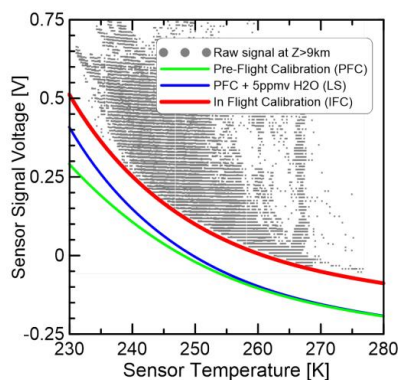


Figure 2. Raw signal of the MOZAIC humidity sensor aboard one MOZAIC aircraft as a function of the sensor temperature inside the aeronautic housing obtained at cruise altitude ($z = 9 - 12$ km). Green line: zero signal from pre-flight calibration (PFC); blue line: superposition of zero signal from PFC and contribution by 5 ppmv water vapour; red line: zero signal from In-Flight Calibration (IFC).

during the respective flight sequence. In case of a sensor offset drift during MCH operation, the lower envelope from the P01 values is similar to the baseline for dry conditions at calibration plus the 5 ppmv stratospheric H_2O background value, but shifted by a voltage offset. The difference between the lower envelope and the baseline from calibration determines the sensor offset voltage which is then subtracted from the raw signal. Details of the methodology are described in detail by Smit et al. (2008).

2.4 RH data validation

The IFC method was applied to the full reanalysis data set from 1995 to 2010. Figure 3a illustrates the effect of the IFC method for the averaged RH_{ice} PDF from the entire MOZAIC period, calculated from annual PDFs.

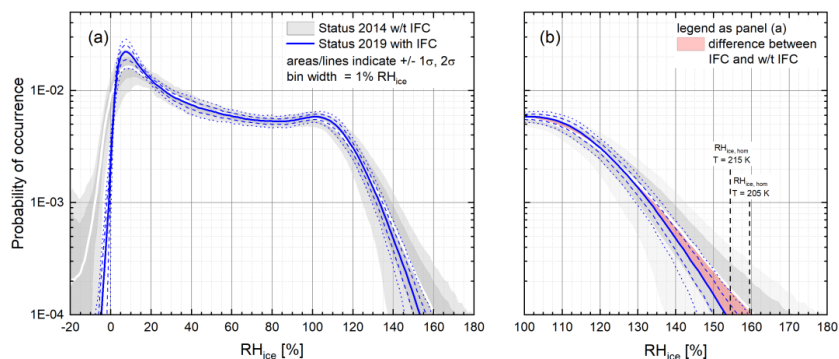


Figure 3. Averaged probability density functions of RH_{ice} for the entire MOZAIC period from 1995 to 2010 (a) and the zoom into the region of ice-supersaturation (b); data stem from the reanalysis (Smit et al., 2014) without (white line, grey areas), and with (blue lines) the in-flight calibration method applied to the data; red-shaded area indicates the difference between IFC applied and not applied, and vertical lines indicate the threshold RH_{ice} values for homogeneous nucleation of ice at $T = 205$ K and $T = 215$ K (Koop et al., 2000).



Solid lines refer to the MOZAIC average PDF without the IFC method (white) and with the IFC method applied
 240 (blue). Grey areas (without IFC) and dashed and dotted blue lines (with IFC applied) represent the $\pm 1\sigma$ and $\pm 2\sigma$
 ranges. Figure 3b shows a zoom into the PDF for the range with $RH_{ice} > 100\%$. In addition to Panel (a), the red
 area marks the difference between the averaged PDFs without and with IFC applied.

The overall features of the RH_{ice} PDF with an overall maximum value at dry stratospheric air mass values with
 RH_{ice} being close to the LOD of approx. 10%, and a second local maximum at $RH_{ice} \approx 100\%$ for observations
 245 inside cirrus clouds remain unaffected, whereas the deviation between the average PDFs becomes relevant for
 RH_{ice} values above 130%. Here, the IFC leads to an average reduction of $< 5\%$ RH_{ice} for an occurrence
 probability of 10^{-3} and approx. 7.5% RH_{ice} for an occurrence probability of 10^{-4} . More relevant, the 2σ -
 variability of the observed ice-supersaturations at 10^{-4} occurrence probability reduces from max. 180% RH_{ice}
 (without IFC) to 155% RH_{ice} (with IFC). The latter value with the IFC applied fits in the range of the
 250 homogeneous freezing thresholds at typical extratropical tropopause conditions of $RH_{ice,hom} = 158.25\%$ at 205 K
 to $RH_{ice,hom} = 154.15\%$ at 215 K (Koop et al., 2000), as sampled by MOZAIC. Respective values without the IFC
 applied, however, exceed the homogeneous nucleation threshold significantly. Figure 4 illustrates the
 distribution of RH_{ice} observations as a function of ambient temperature, colour-coded by the probability of
 occurrence. Obviously, RH_{ice} observations remain inside the physical boundaries let by the water saturation line
 255 and the line for homogeneous ice nucleation.

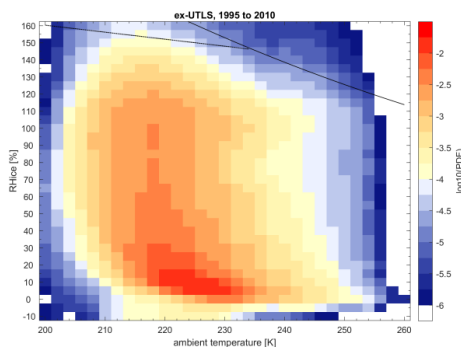


Figure 4. Distribution of RH_{ice} for the entire MOZAIC period from 1995 to 2010 as a function of ambient
 temperature with the colour indicating the probability of occurrence; the lines represent water saturation (solid
 line; Sonntag, 1994) and the threshold RH_{ice} for homogeneous ice nucleation (dotted line; Koop et al., 2000;
 260 Kärcher and Lohmann, 2002).

Besides the validation of MOZAIC RH_{ice} distributions with respect to the homogeneous nucleation thresholds
 from (Koop et al., 2000), the data were compared to the distribution of RH_{ice} from observations on board of
 research aircraft by high-precision water vapour instruments such as Lyman- α photo-fragment fluorescence
 265 hygrometers (Zöger et al., 1999; Sitnikov et al., 2007), tunable diode laser absorption spectrometers (May and
 Webster, 1993; Krämer et al., 2009; Buchholz et al., 2013), and frost point hygrometers; see Meyer et al. (2015)
 for details. In total, 250 research flights from 32 field campaigns conducted between 1999 and 2017 were
 analysed. To ensure comparability to the MOZAIC data set, the temperature range was restricted to 205 K to 235
 K which corresponds to the MOZAIC observation range, with the upper temperature limit set by the
 270 homogeneous freezing threshold.

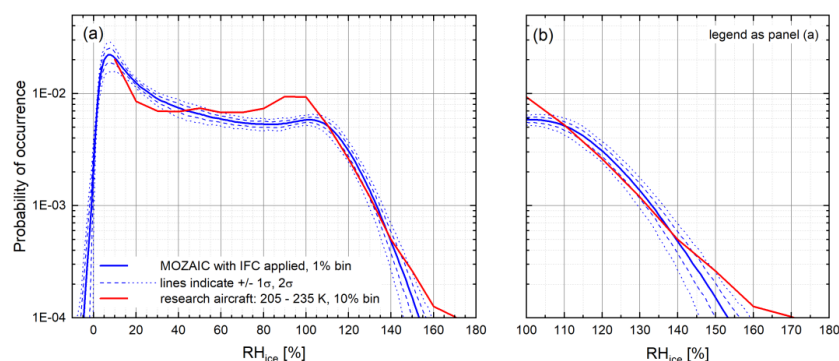


Figure 5. Averaged probability density functions of RH_{ice} for the entire MOZAIC period from 1995 to 2010; with the in-flight calibration method applied (blue lines) and respective RH_{ice} PDF from 250 research aircraft flights collected in the Juelich In-situ Airborne Database (Krämer et al., 2016).

275

The result of this validation is shown in Figure 5. The MOZAIC RH_{ice} PDF are plotted similar to Figure 3, whereas the RH_{ice} PDF from the research aircraft campaigns is shown as red line, calculated for RH_{ice} bin widths of 10%. Both probability distribution functions show excellent agreement within the uncertainty ranges, particularly for the regime of ice-supersaturation (panel b). The differences for RH_{ice} near 100% are caused by the preferred sampling of ice clouds during the field campaigns (higher probability of ice clouds at $RH_{ice} \approx$

280

100%) and by frequent sampling of contrails at subsaturated conditions ($RH_{ice} < 100\%$). RH_{ice} observations from the CARIBIC passenger aircraft exhibit similar features as the observations shown here from MOZAIC and from research aircraft, with maximum probability of occurrence at $RH_{ice} = 100\%$ and maximum RH_{ice} values of approx. 150% (Dyroff et al., 2014). In that respect, all observation platforms provide

285

consistent information on the distribution of ice-supersaturation in the extratropical tropopause. With the IFC method applied to the full MOZAIC RH_{ice} data, this data set is successfully validated against RH_{ice} observations by high-precision instruments and against physically justified bounding values. In summary, this data set is considered of highest possible quality achievable by this kind of routine observations.

3 Results

290

3.1 Annual cycles of water vapour and RH_{ice} distributions at the tropopause

The annual cycles of the vertical distributions of water vapour volume mixing ratio (H_2O VMR) and RH_{ice} were analysed for the three target regions Eastern North America (ENA), North Atlantic (NAtl) and Europe (EU), based on 15-year averages of monthly mean profiles relative to the thermal tropopause. For all investigated regions, the annual cycles of H_2O VMR vertical distributions are shown in Figure 6. For the lowest layer of the lowermost stratosphere, bounded from below by the thermal tropopause layer, the patterns are similar for the three regions, characterised by low H_2O VMR values in winter and spring months and a maximum H_2O VMR during summer. For all regions, the influence of upper tropospheric air masses reaches approx. 1.0 - 2.0 km above the tropopause, with strongest influence in summer.

295

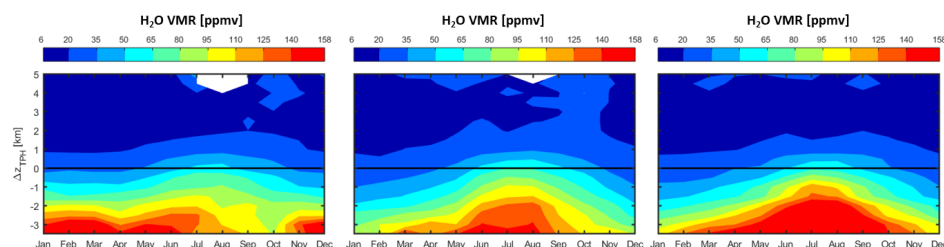


Figure 6. 15-year averaged annual cycles of H₂O VMR vertical distributions of H₂O VMR for latitudes 40 °N to 60 °N and for the regions (from left to right) Eastern North America (105 °W to 65 °W), North Atlantic (65 °W to 5 °W) and Europe (5 °W to 30 °E).

Below the tropopause layer, however, we find different behaviour for the studied regions. It appears that over the North Atlantic and over Europe which is strongly influenced by the North Atlantic synoptic weather systems due to the prevailing westerly winds, the annual cycles of H₂O VMR in the uppermost troposphere and tropopause layers are coupled, while for the Eastern North American region the upper free troposphere layers seem to be more humid in winter than over the ocean. At the tropopause level however, the differences vanish and the annual cycles converge.

A similar behaviour of the annual cycle of H₂O VMR was reported by Zahn et al. (2014) from zonal-averaged H₂O VMR observations by the CARIBIC system. In contrast to MOZAIC, the CARIBIC H₂O sensor provides good data also for the lower stratosphere where the MOZAIC RH sensor loses its sensitivity, but due to its limited regional coverage, the CARIBIC data set cannot provide regional-scale resolution. In that respect, these data sets complement each other with CARIBIC observations backing up the MOZAIC H₂O VMR reported for the atmospheric layers just above the thermal tropopause and MOZAIC providing regional-scale resolution of seasonal patterns which is not possible otherwise.

Potential transport pathways of water vapour into the lowermost stratosphere are not in the scope of this study, and cannot be deduced from the analysis shown in Figure 6, but are discussed in depth elsewhere; see e.g., Gettelman et al. (2011), Zahn et al. (2014) and references given therein. In summary, the seasonal variation of H₂O in the first 1-2 km above the tropopause is controlled by shallow, fast, two-way cross-tropopause mixing which is active around the year and is responsible for the extratropical tropopause mixing layer (Hoor et al., 2004), localized deep convection events which occur mainly in the summer period over continents (Anderson et al., 2012; Schwartz et al., 2013), and the hemisphere-scale effect of the Asian summer monsoon (Santee et al., 2017; Rolf et al., 2018). Strong cases of the deep convection events have been reported particularly for the Central United States with unusually wet conditions in the lowermost stratosphere being associated to these events (Anderson et al., 2017). Our long-term data do not point at a significantly higher humidity over the Eastern North America region in summer compared to the North Atlantic and to Europe. However, it has to be noted that our observations are bounded to the Great Lakes area and further North (see Figure 1 for the areal coverage of MOZAIC observations), whereas the deep convection events with strong overshooting are reported for regions further South over the Great Plains. This regional difference may explain the differing observations.



3.2 Annual cycles of RH_{ice} and ISSR distributions at the tropopause

The core part of our study is focusing on the vertical distribution, seasonality and regional variability of RH_{ice} and ice-supersaturated regions in particular which are linked to the water vapour content of the investigated atmospheric layers. Therefore, we discussed the observed water vapour distribution patterns in the preceding section. To shift the focus on RH_{ice} , Figure 7 represents a similar analysis as shown in Figure 6, but for relative humidity with respect to ice. In contrast to the differing annual cycles of water vapour distributions at the tropopause as discussed above, we find similar patterns for UTH and RH_{ice} over all target regions, with a tropopause layer characterised by mean RH_{ice} of 60% almost independent of the season, a very humid layer just below the tropopause with mean RH_{ice} reaching 80% and weak seasonality, and a stronger seasonality of UTH at approx. 1 km below the tropopause and further down into the upper free troposphere with dryer air during the summer season and very humid conditions particularly during winter and spring. Similar values of RH_{ice} of 60 – 70% for the uppermost troposphere without significant seasonality are reported from CARIBIC observations (Dyroff et al., 2014; Zahn et al., 2014).

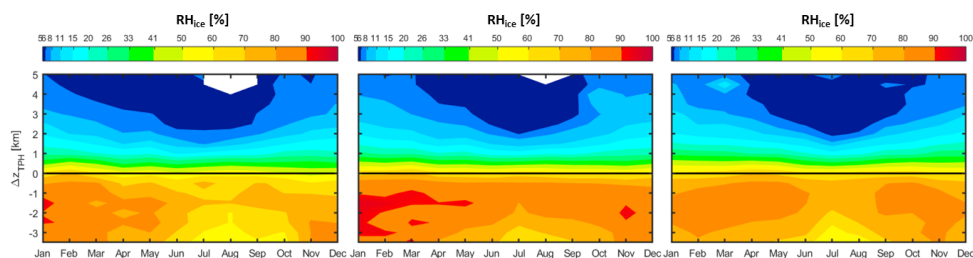


Figure 7. 15-year averaged annual cycles of RH_{ice} for latitudes 40 °N to 60 °N and for the regions (from left to right) Eastern North America (105 °W to 65 °W), North Atlantic (65 °W to 5 °W) and Europe (5 °W to 30 °E).

Grouping the data set shown in Figure 7 into seasonal clusters of layers of 30 hPa thickness around the tropopause allows the robust statistical analysis of the vertical distributions of temperature, H_2O VMR, average RH_{ice} and fraction of ice-supersaturated regions. The applied concept of the vertical spacing is described in Section 2.1. The seasonal variation of the vertical distributions of the selected properties is compiled in Figure 8. Table 1 and Table 2 present the average fractions (Table 1) and associated standard deviations (Table 2) for ISSR occurrence, separated for regions and seasons, and in the last column set averaged over all regions. As is indicated by Figure 7, the variation of RH_{ice} with altitude and season is similar for the three target regions.

For all regions, the highest RH_{ice} values and also the highest fraction of ISSR occurrence is observed for the two upper tropospheric layers closest to the tropopause layer whereas for the third layer situated deepest inside the UT, RH_{ice} values and ISSR fractions are considerably lower. Only in the spring season (MAM) over the North Atlantic, the lowest third layer reaches similar values for RH_{ice} values and ISSR fractions as the two layers above. Interestingly, the standard deviations of ISSR fraction mean values are highest for the lowest layer investigated here, at least for winter and spring seasons for which the largest ISSR fraction is found. The decline in variability with increasing altitude illustrates the damping of the annual cycle of UTH when getting closer to the tropopause layer.

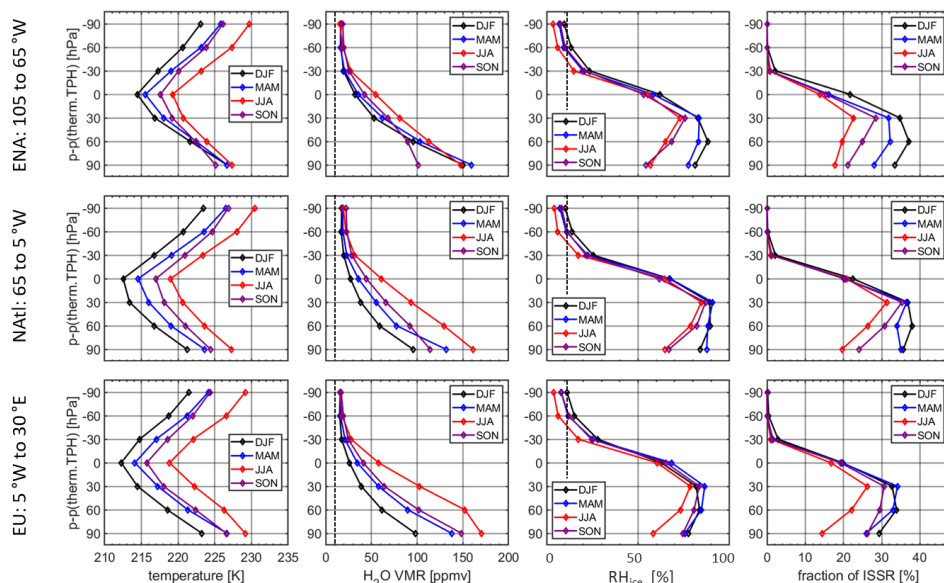


Figure 8. Vertical distribution of mean temperature, H_2O mixing ratio, RH_{ice} and fraction of ice-supersaturated regions (ISSR) for seven pressure layers around the thermal tropopause; layer thickness is 30 hPa and layers are spaced equally relative to the tropopause pressure level; dotted lines indicate the MCH 2- σ limit of detection of $RH_{ice,LOD} = 12\%$ and the resulting minimum-detectable H_2O VMR of approx. 10 ppmv.

Table 1. ISSR occurrence probability: seasonal average values are reported in %, the vertical distance to the thermal tropopause is reported as $\Delta p = p(\text{layer}) - p(\text{thermal TP})$.

Δp (hPa)	DJF			MAM			JJA			SON			AVG			
	ENA	NAtl	EU	ENA	NAtl	EU	ENA	NAtl	EU	ENA	NAtl	EU	DJF	MAM	JJA	SON
-30	2.1	2.2	2.9	0.7	1.2	1.5	0.6	0.9	1.0	0.8	1.2	1.3	2.4	1.1	0.8	1.1
0	21.7	22.4	19.8	16.2	20.1	19.5	13.8	20.8	16.7	15.5	20.4	19.2	21.3	18.6	17.1	18.4
30	34.7	36.8	32.8	31.8	36.5	34.1	22.7	31.3	26.3	28.4	35.3	30.6	34.8	34.2	26.8	31.4
60	37.1	37.9	33.9	32.2	34.0	33.0	19.6	26.4	22.1	25.0	30.8	29.5	36.3	33.0	22.7	28.5
90	33.5	35.7	29.3	28.0	35.0	26.0	17.7	19.6	14.3	21.1	24.1	26.3	32.8	29.6	17.2	23.8

Table 2. ISSR occurrence probability: standard deviation of seasonal average are reported in %, the vertical distance to the thermal tropopause is reported as $\Delta p = p(\text{layer}) - p(\text{thermal TP})$.

Δp (hPa)	DJF			MAM			JJA			SON			AVG			
	ENA	NAtl	EU	ENA	NAtl	EU	ENA	NAtl	EU	ENA	NAtl	EU	DJF	MAM	JJA	SON
-30	2.2	1.6	2.4	0.6	0.5	0.7	0.6	0.5	0.5	0.7	0.4	0.5	2.1	0.6	0.5	0.5
0	5.7	7.0	6.1	5.1	4.3	4.3	4.3	5.1	3.2	3.8	3.3	4.5	6.3	4.6	4.2	3.8
30	5.3	7.3	4.9	6.1	6.6	5.1	7.0	7.7	6.1	4.4	3.4	3.9	5.8	6.0	6.9	3.9
60	6.9	9.1	6.8	8.0	5.7	4.1	6.0	5.9	4.8	4.3	4.0	4.3	7.6	5.9	5.6	4.2
90	9.8	11.0	7.5	5.9	11.5	3.8	3.3	3.6	4.4	6.2	3.6	4.4	9.4	7.1	3.8	4.7



3.3 Physico-chemical signature of ice-supersaturated regions in the vicinity of the tropopause

As discussed in detail by Spichtinger and Leschner (2016) ice-supersaturated air masses have faced decrease in temperature, increase in pressure, or increase in water vapour mixing ratio, i.e. specific humidity, during their past lifetime. Thus, these air parcels are known as both colder and more humid than the embedding sub-saturated air masses (Gierens et al., 1999; Spichtinger et al., 2003b). This conclusion is valid for both ISSR in the uppermost troposphere as well as for the rarer cases of ISSR above the tropopause.

In order to study the formation history of ISSR and involved processes, we analysed the occurrence frequency and physico-chemical signature of ISSR around the tropopause layer and referred our analyses to both the thermal and the dynamical tropopause. We want to recall the tropopause definitions given in Section 2.1. The thermal tropopause according to WMO criteria (WMO, 1957) is usually seen as an effective transport barrier hampering troposphere-stratosphere exchange, whereas the dynamical tropopause is commonly used for separating tropospheric and stratospheric air masses in studies on stratosphere–troposphere transport since it represents the lower bound of the tropopause mixing layer (Gettelman et al., 2011; Ivanova, 2013).

Our analysis is confined to the North Atlantic region, for which we have the highest data density available with respect to vertical resolution. For each season of the 15-years period we calculated the average occurrence probability for ISSRs per altitude layer relative to the thermal tropopause. The PDF of ISSR occurrence per altitude layer was then calculated from this ensemble. For the sake of statistical significance, we skipped the distinction between seasons for this specific analysis and calculated instead median values and respective percentiles for the entire North Atlantic data set. However, seasonal information is contained in the statistical entity via the seasonally averaged ISSR fractions. The results are compiled in Table 3 for both tropopause definitions used here.

With reference to thermal tropopause, the average ISSR occurrence probability is 29% in the troposphere and increases to 34% when approaching the tropopause layer. With reference to the dynamical tropopause, the overall behaviour is similar with an increasing average ISSR occurrence probability when reaching the tropopause layer, but the absolute values are larger since the analysed layers reach deeper into the upper troposphere. For both tropopause definitions, the variability of observed ISSR fractions is largest for the lowest UT layer of the analysed atmospheric region and decreases with increasing altitude.

Table 3. Mean and standard deviation of seasonal fraction of ice supersaturated regions (ISSR) for the seven vertical layers distributed around the thermal and dynamical tropopause.

Layer ID	$p - p_{TPH}$ [hPa]	ISSR fraction [%]	
		Thermal TP	Dynamical TP
LMS3	- 90	0.0±0.1	0.2±0.5
LMS2	- 60	0.1±0.3	0.7±1.1
LMS1	- 30	1.5±1.1	8.4±4.4
TPL	0	20.0±6.5	30.7±9.4
UT1	30	33.9±9.0	39.9±10.0
UT2	60	31.4±9.2	37.7±10.7
UT3	90	29.1±12.1	35.5±14.3



When crossing the thermal tropopause, the ISSR fraction drops sharply to values of 1.5% for the lowest layer above the tropopause and to statistically insignificant fractions when reaching further up into the stratosphere. In case of the dynamic tropopause, we find a significantly higher ISSR fraction of 8.4% for the lowest stratosphere layer, and again insignificant fractions further above. This strong contrast in the ISSR occurrence probability for the lowest stratosphere layers with reference to the two tropopause definitions is caused by the different physical natures of the thermal and dynamic tropopauses. While the thermal tropopause forms a robust barrier for the vertical transport of water vapour, the dynamic tropopause serves as the lower bound for an atmospheric layer characterised by dynamically driven mixing processes (Gettelman et al., 2011). As a consequence, we expect different chemical signatures for the ISSR above the thermal and dynamical tropopauses.

In order to learn more about the history of ice-supersaturated air parcels we further analysed the ozone content of the ISSR compared to the sub-saturated air around, for air parcels below and above the thermal and dynamic tropopauses and combined the results with the distributions of temperature and H₂O VMR. The thermodynamic and chemical properties of ISSR and the comparison between ISSR (blue lines) and ice-sub-saturated air masses (red-shaded areas and red lines) are presented in Figure 9 with reference to both tropopause definitions. In general, ISSR are colder than their subsaturated counterparts. The difference is low in the UT with 1 - 2 K which compares well to the value of 2 K at 215 hPa obtained from MLS satellite measurements (Spichtinger et al., 2003b), and increases to more than 6 K difference in the stratosphere above the thermal tropopause, and approx. 4 K above the dynamic tropopause. The temperature difference of 3 - 4 K between colder tropospheric ISSR and the surrounding subsaturated air masses reported by Gierens et al. (1999) is comparable to the temperature difference in the 30 hPa thick tropopause layer we find in our analysis.

Figure 9 also indicates a similar behaviour of the vertical distribution of H₂O VMR for ice-supersaturated and ice-sub-saturated regions with exponentially decreasing absolute humidity up to the tropopause layer. Above both tropopause layers, it further decreases for the non-ISSR, whereas the water vapour VMR remains constant with height at the tropopause layer value of about 55 ppmv in the case of ISSR just above the tropopause. The increase of H₂O VMR in the tropopause ISSR by more than a factor of 2 is comparable to the results of MLS observations (Spichtinger et al., 2003b), while Gierens et al. (1999) reported an increase of only 50% for water vapour VMR in ISSR compared to non-ISSR, which compares well to our observations in the uppermost troposphere.

The vertical distribution of the ozone VMR behaves similar to the temperature for ice-supersaturated and ice-sub-saturated regions, with small differences in the ozone VMR of less than 15 ppbv in the troposphere. Already for the tropopause layer and even more pronounced for the first layer above the thermal tropopause, however, the difference increases to 60 ppmv ozone VMR and beyond.

Quantitative conclusions on air mass characteristics and history are drawn from the vertical distributions of thermodynamic and chemical properties shown in Figure 9. The underlying concept of troposphericity (Cirisan et al., 2013) quantifies the tropospheric nature or fingerprint, respectively, of an air mass on the basis of the observed O₃ VMR. In the context of our study, we refer to troposphericity for consistency with literature.

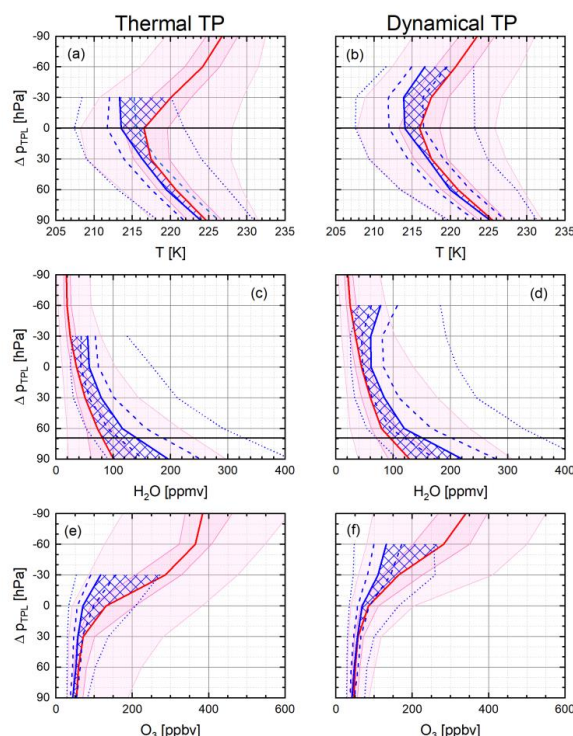


Figure 9. Vertical distribution of temperature, H₂O VMR, and ozone VMR for ISSR relative to the thermal tropopause (panels a, c and e) and 2 PVU dynamical tropopause (panels b, d, and f). ISSR conditions are presented as percentiles [1, 25, 50, 75, and 99] by blue lines and non-ISSR conditions by red-shaded areas; blue cross-hatched areas highlight the deviation of median values inside ISSR from those non-ISSR conditions.

Using the ozone volume mixing ratio as a stratospheric air mass tracer and adapting their approach, we define the troposphericity parameter m for an ensemble of data characterised by median (med) and 99 percentile (P99) values as

$$m = \frac{[O_3]_{P99} - [O_3]_{med}}{[O_3]_{P99} - [O_3]_{tropo}}$$

and apply the median value of the lowest layer analysed here as background tropospheric value, so that $[O_3]_{tropo} = 42$ ppbv. Petetin et al. (2018) reported a median O₃ VMR of 49 ppbv for the Central European mountain station Sonnblick (3106 m above sea level) in the Austrian Alps and a value 50 ppbv for the high Alpine station Jungfraujoch (3580 m above sea level), whereas Cirisan et al. (2013) use a value of 33.5 ppbv from ERA Interim air mass trajectory analyses.

Applying this definition of the troposphericity parameter m to MOZAIC/IAGOS observations over Central Europe (Petetin et al., 2018) at 4000 m altitude with $[O_3]_{med} = 50$ ppbv and $[O_3]_{P99} = 82$ ppbv yields $m = 0.80$, and for observations at 1500 m altitude with $[O_3]_{med} = 42$ ppbv and $[O_3]_{P99} = 83$ ppbv we find $m = 1.00$.



For MOZAIC/IAGOS observations in the Ex-UTLS Cohen et al. (2018) report, e.g., for springtime lowermost stratosphere conditions values of $[O_3]_{med} = 400$ ppbv and $[O_3]_{P95} = 600$ ppbv, resulting in $m = 0.36$, and for tropopause layer conditions values of $[O_3]_{med} = 110$ ppbv, $[O_3]_{P95} = 200$ ppbv, and $m = 0.57$; note that P95 refers here to the 95 percentile value of the analysed data ensemble. Deeper into the stratosphere beyond the reach of MOZAIC/IAGOS aircraft, the value of m approaches $m = 0.0$. Thus, similar to the troposphericity parameter defined by Cirisan et al. (2013) from trajectory analyses, a value of $m = 0$ indicates that an air parcel contains only stratospheric air, while $m = 1$ is fully tropospheric. Defining the troposphericity as described here, we connect the troposphericity of an air mass to the observed variability of the O_3 VMR.

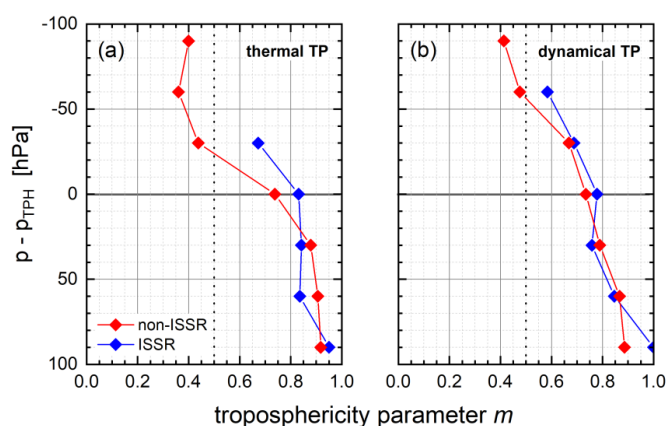


Figure 10. Vertical distribution of the troposphericity parameter m for ISSR and non-ISSR air masses with respect to the thermal (a) and dynamical (b) tropopause.

The analysis of troposphericity of the seven investigated layers with respect to the 99 percentile and median O_3 VMR is presented in Figure 10. With respect to the thermal as well as to the dynamical tropopause, the layers up to the tropopause layer are characterised by almost similar values of $m > 0.80$ for ISSR and $m > 0.75$ for non-ISSR air masses. The first layer above the thermal tropopause, however, shows a clear difference between ISSR ($m = 0.67$) and non-ISSR ($m = 0.44$) with respect to the thermal tropopause, but similar values of $m = 0.67 - 0.69$ for ISSR and non-ISSR with respect to the dynamical tropopause.

With respect to the thermal tropopause, we find a distinct difference in the mixing behaviour. Above the transport barrier formed by the thermal tropopause, non-ISSR air masses show a clear stratospheric signature. In contrast, ISSR air masses just above the tropopause are still strongly influenced by mixing and of significant tropospheric nature compared to the non-ISSR air masses. Referring to the dynamical tropopause, the influence of mixing increases gradually for both ISSR and non-ISSR air masses and the difference in troposphericity is much less pronounced than in the case of the thermal tropopause.

Concluding, for both tropopause definitions used in our analysis, the troposphericity values indicate continuing tropospheric influence for ISSR inside and above the respective tropopause layer. For the non-ISSR, however, the stratospheric nature is clearly visible above the thermal tropopause whereas above the dynamical tropopause the air masses show still a relevant tropospheric influence. All investigated properties demonstrate the efficiency of the thermal tropopause as a vertical transport barrier, while the air masses between the dynamical and the thermal tropopauses are clearly shaped by mixing with tropospheric air.



3.4 ISSR fraction and cirrus cloud occurrence

Ice-supersaturation in the atmosphere is a prerequisite for the formation of cirrus clouds, and the degree of supersaturation, mostly driven by atmospheric dynamics determines the mechanism by which ice particles form (e.g., Kärcher et al., 2014; Krämer et al., 2016; Heymsfield et al., 2017). Ice-supersaturation can also occur in cloud-free air masses, but the fraction of ice-supersaturated air in clear sky conditions is largely unknown. However, these cloud-free ISSR are of high importance for the formation of persistent contrails and thus for the climate impact of aviation (Irvine and Shine, 2015; Kärcher, 2018).

Driven by the high importance of ISSR for cirrus formation and existence and also for the formation and persistence of contrails, we converted the vertically resolved observations of ISSR fractions into an annual cycle of ISSR occurrence for the three target regions. The seasonal-mean occurrence probabilities were analysed for RH_{ice} values of 95%, 100% and 105%, based on the sensor precision of 5% RH_{ice} . The resulting annual cycles for the top UT layer, situated just below the tropopause layer are shown in Figure 11. The range bound by the probabilities of occurrence for $RH_{ice} = 95\%$ and 105% defines the uncertainty of our analysis. Additionally, we analysed the interannual variability of ISSR occurrence from the standard deviation of the mean ISSR occurrence probability for $RH_{ice} = 100\%$. The respective variability range is shown as blue-shaded areas in Figure 11. It becomes clearly visible, that the sensor uncertainty and the interannual variability of the ISSR occurrence probability cover similar ranges.

For all regions, ISSR occurrence probabilities are highest in winter/spring and lowest in summer, while the absolute values particularly in summer are considerably different. The probability for finding ice-supersaturated air masses during summer is 20% over the Eastern North America regions, but 30% over the North Atlantic, with Europe showing values in the range between.

To the present, there is only very limited in-situ information available about the occurrence probability of ice-supersaturated air masses in the upper troposphere in general and about their seasonality in particular. One source for in-situ information stems from radiosonde observations conducted by the German Weather Service over the observatory Lindenberg in Germany (Spichtinger et al., 2003a).

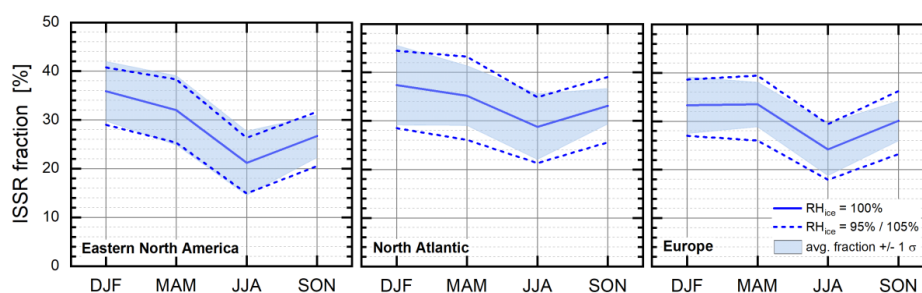


Figure 11. Annual cycles of ISSR occurrence shown as occurrence probability for $RH_{ice} > 100\%$, for the regions Eastern North America, North Atlantic and Europe; considered years are 1995 to 2010, with shaded areas representing probabilities for the average value (thick lines) $\pm 1\sigma$, and the short-dashed lines representing average fractions for $RH_{ice} = 95\%$ and 105%, respectively; calculations were conducted for the two UT layers positioned closest to the tropopause.

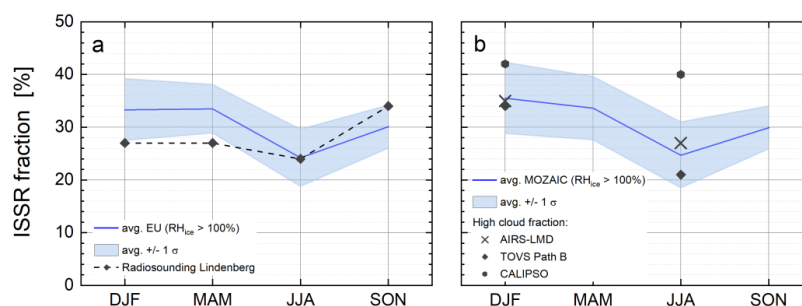


Figure 12. a: Seasonal cycle of ISSR occurrence probability, i.e. $p(\text{RH}_{\text{ice}} > 100\%)$, averaged over Europe for the years 1995 to 2010; symbols represent the annual cycle of the Lindenberg sounding (2000 – 2001) from Spichtinger et al. (2003a); b: Seasonal cycle of ISSR occurrence probability, as $p(\text{RH}_{\text{ice}} > 100\%)$ averaged over the Northern Mid-Latitudes from East North America to Europe for the period 1995 to 2010; symbols represent high cloud fractions from the satellite cloud climatology by Stubenrauch et al. (2010) for northern mid-latitudes and years 2003 to 2008 for AIRS-LMD, 1987 to 1995 for TOVS Path B and 2006 to 2007 for CALIPSO.

Figure 12a shows the average annual cycles of ISSR occurrence frequency from 15 years of MOZAIC observations over Europe and from 15 months of radiosonde observations over Lindenberg. The single annual cycle from the radio soundings fits well into the 15 years climatology of ISSR occurrence from MOZAIC. More quantitatively, the authors report a mean frequency of occurrence of ice-supersaturation layers over Lindenberg of 28%, whereas the annual cycle of ISSR occurrence from our MOZAIC observations over Europe yields a mean value of 29.5% with a range from 35% ($\text{RH}_{\text{ice}} = 95\%$) to 23% ($\text{RH}_{\text{ice}} = 105\%$).

Another source of data, but for the occurrence frequency of cirrus clouds originates from long-term analyses of satellite observations (Stubenrauch et al., 2010; Stubenrauch et al., 2013). In their 6-year climatology Stubenrauch et al. (2010) report cirrus cloud coverage fractions for northern mid-latitudes of 35% in January and 27% in July from AIRS-LMD (2003 to 2008), and respective fractions of 34% and 21% from TOVS – Path B (1987 to 1995), and 42% and 40% from CALIPSO (2006 to 2007). The compilation of our annual cycle of ISSR occurrence and the respective observations from space-borne sensors is shown in Figure 12b. The agreement of the observations of ISSR occurrence from the very different sources is remarkably good, with the exception of CALIPSO observations which provide higher values. It has to be noted, however, that CALIPSO also detects subvisible cirrus clouds which are below the detection limit of the other instruments.

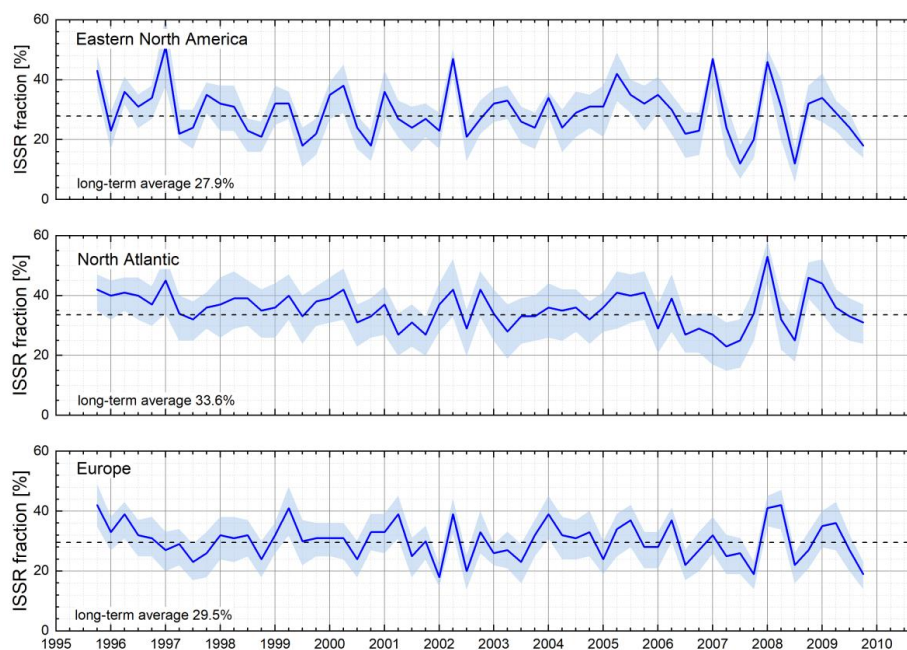
The close match between MOZAIC in-situ observations of RH_{ice} with the high-cloud fraction from satellite instruments corresponds to the finding from other studies that by far the largest part of ISSRs occurs inside cirrus clouds. We find from the analysis of a large set of combined observation of RH_{ice} and ice crystal number concentration N_{ice} during a series of research flights (approx. 68000 observations of ice-supersaturation; Krämer et al., 2016), that approx. 80 % of the observed ice-supersaturation events are associated with in-cloud conditions. First exemplary analyses of simultaneous observations of RH_{ice} and N_{ice} which are now possible within the ongoing IAGOS programme also indicate a strong correlation of high RH_{ice} values with its occurrence inside cirrus clouds (Petzold et al., 2017). Further studies on this topic will be launched as soon as the full data set of combined observations of RH_{ice} and N_{ice} from IAGOS flights since 2011 is validated.



555 3.5 Trend analysis

Finally, we analysed the 15-years records of the validated MOZAIC RH_{ice} observations and the resulting fraction of ISSR observations for the three regions Eastern North America, North Atlantic and Europe for potential trends. The bases of our analyses were the seasonally averaged observations in the uppermost tropospheric layer (UT) and the respective average seasonal cycles depicted Figure 11. The resulting time series are shown in
 560 Figure 13. The seasonality of ISSR occurrence is clearly visible for each region, but with considerable interannual variability. Similar to Figure 11, the shaded regions represent the average fractions for $RH_{ice} = 95\%$ and 105% , respectively, and indicate thus the uncertainty resulting from the instrument precision of $RH_{ice} = 5\%$. For none of the regions, we find significant trends in ISSR occurrence. Therefore, the distribution of RH_{ice} in the uppermost troposphere close to the tropopause layer and the resulting occurrence of ice-supersaturation seem to
 565 be stable over the investigated time period from 1995 to 2010.

In order to get a clearer understanding of the reasons for the interannual variability, we further analysed the de-seasonalised time series of the ISSR fractions by calculating the difference between each seasonal value of the ISSR fraction and the 15-years average seasonal cycle (see Figure 11).



570 **Figure 13.** Time series of ISSR fraction (probability of occurrence) for latitudes 40°N to 60°N and for the regions (from top to bottom) Eastern North America (105°W to 65°W), North Atlantic (65°W to 5°W) and Europe (5°W to 30°E) with the solid lines representing probabilities for the average value for $RH_{ice} = 100\%$ and the shaded areas representing average fractions for $RH_{ice} = 95\%$ and 105% , respectively; long-term average values for $RH_{ice} = 100\%$ are added in the panels.

575

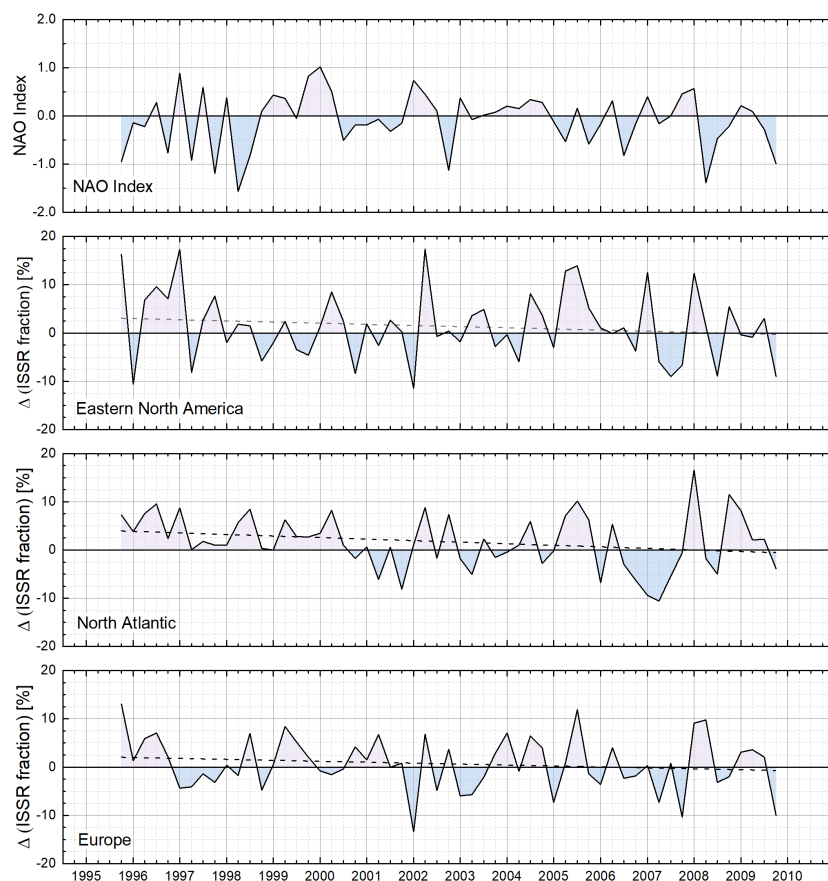


Figure 14. De-seasonalised time series of ISSR fraction (probability of occurrence) for latitudes 40°N to 60°N and for the regions (from top to bottom) Eastern North America (105°W to 65°W), North Atlantic (65°W to 5°W) and Europe (5°W to 30°E).

580

The de-seasonalised time-series thus positive and negative deviations from the long term average values. The resulting time series are presented in Figure 14. As for the time series of ISSR occurrence, we performed a trend analysis and added the obtained trend lines to Figure 14. Respective decadal slopes are $-1.95\% \pm 1.77\%$ for Eastern North America, $-3.21\% \pm 1.78\%$ for the North Atlantic, and $-2.39\% \pm 2.29\%$ for Europe and indicated

585

uncertainties of the determined slopes refer to one standard deviation. Thus none of the slopes differs significantly from zero, and similar to the time series of ISSR occurrence, we do not observe significant trends for the seasonal deviation of ISSR occurrence from the long-term average for the three target regions.

One potential weather phenomenon driving the deviation of seasonal ISSR occurrence from the long-term average in the investigated region is the North Atlantic Oscillation (NAO). The NAO index describes the deviation of the pressure difference between the Iceland low and the Azores high pressure systems from long-term average value. As an example, a positive value of the NAO index indicates that Δp (Iceland L to Azores H)

590

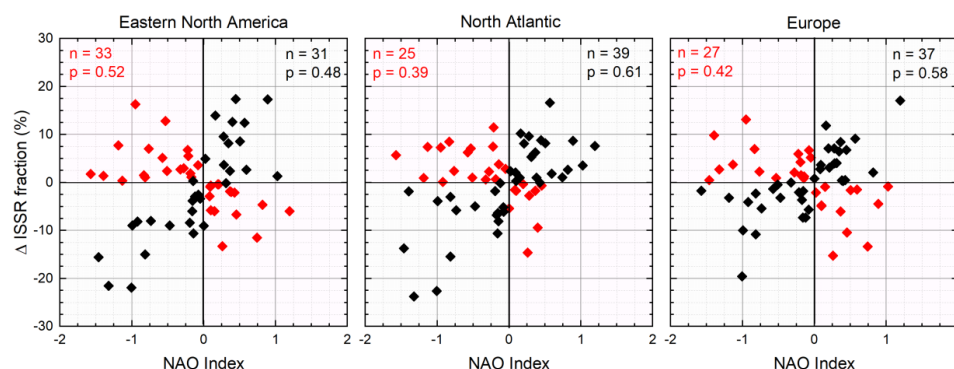


Figure 15. Cluster analysis with respect to the correlation of signs between NAO index and deviation of ISSR occurrence from the long-term average (Δ ISSR) for the target regions; black symbols and grey shaded clusters indicate the same sign for NAO index and Δ ISSR, red symbols and red shaded clusters indicate opposite signs.

is larger than on average. This larger pressure difference causes stronger westerly winds and thereby more active storm tracks over the North Atlantic which brings warmer and more moist air to Europe. Under such conditions we would expect a higher probability of ice-supersaturation in the uppermost troposphere. Such a positive correlation between NAO and cirrus cloud cover is reported from an analysis of cirrus cloud cover data from the International Satellite Cloud Climatology Project and relative humidity data from ECMWF/ERA40 by Eleftheratos et al. (2007).

To investigate this potential link, we added the seasonally averaged NAO index to Figure 14 (top panel). Since there is no immediate evidence given for a link between the NAO index and the deviation of ISSR occurrence from the long-term average, we further searched for a potential link of signs in the sense that positive and negative NAO index values are associated to positive and negative deviations of ISSR occurrence from the long-term average, respectively. The results of this cluster analysis are presented in Figure 15.

For the region Eastern North America the probability of cross-correlated signs between NAO index and Δ ISSR fraction is 52% ($p = 0.52$) whereas the probability for correlated signs is 48% ($p = 0.48$). The probabilities are almost equal for this region and from that result we conclude that there is no link between NAO index and Δ ISSR fraction over the eastern part of North America. In contrast, the results are different for the regions North Atlantic and Europe, both of which show correlated signs between NAO index and Δ ISSR in 61% and 58% of the analysed seasons, respectively. For these regions, we consider the correlation of signs statistically significant. The obtained correlation of signs is in line with the observation that the occurrence of ice-supersaturation is well correlated with the storm track activity (Spichtinger et al., 2003b; Gettelman et al., 2006; Lamquin et al., 2012).

4. Summary and Conclusions

The European Research Infrastructure IAGOS (from 2011) and its predecessor programme MOZAC (1994 - 2010) perform global-scale routine in-situ observations of relative humidity with respect to ice (RH_{ice}) by using instrumented passenger aircraft. The validated RH_{ice} data set from the MOZAC period between 1995 and 2010 was analysed for latitudes $40^\circ N$ to $60^\circ N$ and for the regions Eastern North America ($105^\circ W$ to $65^\circ W$), North Atlantic ($65^\circ W$ to $5^\circ W$) and Europe ($5^\circ W$ to $30^\circ E$) to study the occurrence of ice-supersaturated regions



(ISSR) in the uppermost troposphere and tropopause layers. Determined seasonal cycles agree very well with observations of ISSR occurrence from radio soundings (Spichtinger et al., 2003a) and from satellite observations (Spichtinger et al., 2003b; Lamquin et al., 2012).

The high vertical resolution of the MOZAIC RH_{ice} data set with 30 hPa layer thickness allows the determination of the vertical position of the ice-supersaturated air masses with respect to the thermal tropopause. It occurs that the fraction of ice-supersaturated regions is largest for the atmospheric layers of 60 hPa thickness, directly below the thermal tropopause.

Comparing the ISSR fraction from MOZAIC in-situ observations with the high-cloud fraction from satellite instruments (Stubenrauch et al., 2010) yields remarkably close agreement between the two different observations and supports the interpretation that by far the largest part of the ice-supersaturation occurs inside cirrus clouds. This interpretation is also supported by first exemplary analyses of simultaneous observations of RH_{ice} and ice crystal number density N_{ice} from the ongoing IAGOS programme (Petzold et al., 2017). In addition, the close agreement between satellite-based observations of ice cloud occurrence and the MOZAIC/IAGOS in-situ observations of ice-supersaturation demonstrate the unique contribution, MOZAIC and today IAGOS long-term observations can make to this scientific area, in particular with the detailed seasonality of ISSR occurrence over different regions. Future work will combine RH_{ice} and N_{ice} observations which are now available from IAGOS and link them to AIRS time series.

The finding that ice-supersaturated air is generally colder and more humid and – in case of observation inside or above the tropopause layer - carries less ozone than the surrounding air masses is in close agreement with reported results for temperature and humidity. However, we were also able to use ozone as a tracer for stratospheric air and calculate the troposphericity of ice-supersaturated and subsaturated air masses. The analysis yields a significant impact of tropospheric air even on ISSR observed above the thermal tropopause. The thermodynamic features together with the increased troposphericity indicate vertical mixing in the vicinity of the tropopause layer as one important formation process of ice-supersaturation. Future work in this direction will be conducted, once the full IAGOS data set on RH_{ice} , ozone and ice clouds is validated and available.

Over the investigated period of 15 years, no significant trends are observed, neither for the occurrence of ISSR nor for the deviation of seasonal ISSR occurrence probabilities from the long-term average. This statement is valid for all three investigated regions. Yet, we identify significant correlations of signs between the NAO index and the deviation of seasonal ISSR occurrence probabilities from the long-term average for the North Atlantic and Europe regions, whereas no such correlation was found for the Eastern North America region. The resulting interpretation is that a positive NAO index correlates with increased occurrence of ISSR (positive deviation from the long-term average). This interpretation is in agreement with the understanding that a positive NAO index leads to an increased storm track activity which then generates more frequently ISSR.

Finally, in a concomitant study by Reutter et al. (2019), MOZAIC RH_{ice} observations have been compared to ECMWF ERA-Interim data and significant deviations are reported for ice-supersaturated conditions, both in number and strength of supersaturation. The high quality and very good resolution of MOZAIC and later IAGOS RH_{ice} observations will certainly help to further improve the representation of ice-supersaturation in ERA 5 as well as in numerical weather and climate forecasting models.



Author contributions

665 AP designed the study and prepared the manuscript, with contributions from all co-authors; PN, SR, MR, and HGJS performed the quality control and analysis of MOZAIC/IAGOS water vapour data; FB provided the thermal tropopause pressure levels and performed the quality control and analysis of temperature data; MK and NS contributed the analysis of the research aircraft data. PNed performed the quality control and analysis of ozone data; AW and PS contributed to the interpretation of the study results.

670

Competing interests

The authors declare that they have no conflict of interest.

Data Availability

675 The IAGOS data are available at <https://doi.org/10.25326/20>.

We used the following data versions for our analyses:

Version 1.0 of IAGOS air_temp and air_stag_temp data, based on the method described in Helten et al. (1998).

Version 3.0 of IAGOS RHL, RHI and H₂O_gas data, based on the calibration techniques and data inversion algorithms published in Helten et al. (1998). In addition, version 3.0 has implemented the in-flight calibration
680 technique adapted from Smit et al. (2008), which adjusts for an offset drift of the MCH sensor during a flight period.

Acknowledgements

Parts of this study were funded by the German Ministry for Education and Research (BMBF) under Grant No.

685 01LK1301A as part of the joint research programme IAGOS Germany. MOZAIC/IAGOS data are created with support from the European Commission, national agencies in Germany (BMBF), France (MESR), and the UK (NERC), and the IAGOS member institutions (<http://www.iagos.org/partners>). The participating airlines (Deutsche Lufthansa, Air France, Austrian, China Airlines, Iberia, Cathay Pacific, Air Namibia, Sabena) supported IAGOS by carrying the measurement equipment free of charge since 1994. The data are available at
690 <https://doi.org/10.25326/20> thanks to additional support from AERIS. MK thanks JGU Mainz for support as a GFK fellow.

References

- Aaltonen, V., Lihavainen, H., Kerminen, V. M., Komppula, M., Hatakka, J., Eneroth, K., Kulmala, M., and Viisanen, Y.: Measurements of optical properties of atmospheric aerosols in Northern Finland, Atmos. Chem.
695 Phys., 6, 1155-1164, 2006.
- Anderson, J. G., Wilmouth, D. M., Smith, J. B., and Sayres, D. S.: UV Dosage Levels in Summer: Increased Risk of Ozone Loss from Convectively Injected Water Vapor, Science, 337, 835-839, doi: 10.1126/science.1222978, 2012.
- Anderson, J. G., Weisenstein, D. K., Bowman, K. P., Homeyer, C. R., Smith, J. B., Wilmouth, D. M., Sayres, D.
700 S., Klobas, J. E., Leroy, S. S., Dykema, J. A., and Wofsy, S. C.: Stratospheric ozone over the United States in summer linked to observations of convection and temperature via chlorine and bromine catalysis, Proc. Natl. Acad. Sci. U. S. A., 114, E4905-E4913, doi: 10.1073/pnas.1619318114, 2017.



- Berkes, F., Neis, P., Schultz, M. G., Bundke, U., Rohs, S., Smit, H. G. J., Wahner, A., Konopka, P., Boulanger, D., Nédélec, P., Thouret, V., and Petzold, A.: In situ temperature measurements in the upper troposphere and lowermost stratosphere from 2 decades of IAGOS long-term routine observation, *Atmos. Chem. Phys.*, 17, 12495-12508, doi: 10.5194/acp-17-12495-2017, 2017.
- Bock, L., and Burkhardt, U.: Contrail cirrus radiative forcing for future air traffic, *Atmos. Chem. Phys.*, 19, 8163-8174, doi: 10.5194/acp-19-8163-2019, 2019.
- Boucher, O., Randall, D., Artaxo, P., Bretherton, C., Feingold, G., Forster, P., Kerminen, V.-M., Kondo, Y., Liao, H., Lohmann, U., Rasch, P., Satheesh, S. K., Sherwood, S., Stevens, B., and Zhang, X. Y.: Clouds and Aerosols, in: *Climate Change 2013: The Physical Science Basis. Contribution of Working Group I to the Fifth Assessment Report of the Intergovernmental Panel on Climate Change*, edited by: Stocker, T. F., D. Qin, Plattner, G.-K., Tignor, M., Allen, S. K., Boschung, J., Nauels, A., Xia, Y., Bex, V., and Midgley, P. M., Cambridge University Press, Cambridge, United Kingdom and New York, NY, USA, 2013.
- Brenninkmeijer, C. A. M., Crutzen, P. J., Fischer, H., Gusten, H., Hans, W., Heinrich, G., Heintzenberg, J., Hermann, M., Immelmann, T., Kersting, D., Maiss, M., Nolle, M., Pitscheider, A., Pohlkamp, H., Scharffe, D., Specht, K., and Wiedensohler, A.: CARIBIC - Civil aircraft for global measurement of trace gases and aerosols in the tropopause region, *J. Ocean. Atmos. Technol.*, 16, 1373-1383, doi: 10.1175/1520-0426(1999)016<1373:ccafgm>2.0.co;2, 1999.
- Brenninkmeijer, C. A. M., Crutzen, P., Boumard, F., Dauer, T., Dix, B., Ebinghaus, R., Filippi, D., Fischer, H., Franke, H., Friess, U., Heintzenberg, J., Helleis, F., Hermann, M., Kock, H. H., Koepfel, C., Lelieveld, J., Leuenberger, M., Martinsson, B. G., Miemczyk, S., Moret, H. P., Nguyen, H. N., Nyfeler, P., Oram, D., O'Sullivan, D., Penkett, S., Platt, U., Pupek, M., Ramonet, M., Randa, B., Reichelt, M., Rhee, T. S., Rohwer, J., Rosenfeld, K., Scharffe, D., Schlager, H., Schumann, U., Slemr, F., Sprung, D., Stock, P., Thaler, R., Valentino, F., van Velthoven, P., Waibel, A., Wandel, A., Waschitschek, K., Wiedensohler, A., Xueref-Remy, I., Zahn, A., Zech, U., and Ziereis, H.: Civil Aircraft for the regular investigation of the atmosphere based on an instrumented container: The new CARIBIC system, *Atmos. Chem. Phys.*, 7, 4953-4976, 2007.
- Buchholz, B., Kuehnreich, B., Smit, H. G. J., and Ebert, V.: Validation of an extractive, airborne, compact TDL spectrometer for atmospheric humidity sensing by blind intercomparison, *Appl. Phys. B*, 110, 249-262, doi: 10.1007/s00340-012-5143-1, 2013.
- Burkhardt, U., Kärcher, B., Ponater, M., Gierens, K., and Gettelman, A.: Contrail cirrus supporting areas in model and observations, *Geophys. Res. Lett.*, 35, doi: 10.1029/2008gl034056, 2008.
- Burkhardt, U., and Kärcher, B.: Global radiative forcing from contrail cirrus, *Nature*, 1, 54-58, doi: doi:10.1038/NCLIMATE1068, 2011.
- Chen, T., Rossow, W. B., and Zhang, Y. C.: Radiative effects of cloud-type variations, *J. Clim.*, 13, 264-286, doi: 10.1175/1520-0442(2000)013<0264:Reoctv>2.0.Co;2, 2000.
- Cirisan, A., Spichtinger, P., Luo, B. P., Weisenstein, D. K., Wernli, H., Lohmann, U., and Peter, T.: Microphysical and radiative changes in cirrus clouds by geoengineering the stratosphere, *J. Geophys. Res.-Atmos.*, 118, 4533-4548, doi: 10.1002/jgrd.50388, 2013.
- Cohen, Y., Petetin, H., Thouret, V., Marécal, V., Josse, B., Clark, H., Sauvage, B., Fontaine, A., Athier, G., Blot, R., Boulanger, D., Cousin, J. M., and Nédélec, P.: Climatology and long-term evolution of ozone and carbon monoxide in the upper troposphere-lower stratosphere (UTLS) at northern midlatitudes, as seen by IAGOS from 1995 to 2013, *Atmos. Chem. Phys.*, 18, 5415-5453, doi: 10.5194/acp-18-5415-2018, 2018.



- Dee, D. P., Uppala, S. M., Simmons, A. J., Berrisford, P., Poli, P., Kobayashi, S., Andrae, U., Balmaseda, M. A.,
 745 Balsamo, G., Bauer, P., Bechtold, P., Beljaars, A. C. M., van de Berg, L., Bidlot, J., Bormann, N., Delsol, C.,
 Dragani, R., Fuentes, M., Geer, A. J., Haimberger, L., Healy, S. B., Hersbach, H., Holm, E. V., Isaksen, I.,
 Kallberg, P., Kohler, M., Matricardi, M., McNally, A. P., Monge-Sanz, B. M., Morcrette, J. J., Park, B. K.,
 Peubey, C., de Rosnay, P., Tavolato, C., Thepaut, J. N., and Vitart, F.: The ERA-Interim reanalysis:
 configuration and performance of the data assimilation system, *Q. J. R. Meteorol. Soc.*, 137, 553-597, doi:
 750 10.1002/qj.828, 2011.
- Dyroff, C., Zahn, A., Christner, E., Forbes, R., Tompkins, A. M., and van Velthoven, P. F. J.: Comparison of
 ECMWF analysis and forecast humidity data with CARIBIC upper troposphere and lower stratosphere
 observations, *Q. J. R. Meteorol. Soc.*, doi: 10.1002/qj.2400, 2014.
- Eleftheratos, K., Zerefos, C. S., Zanis, P., Balis, D. S., Tselioudis, G., Gierens, K., and Sausen, R.: A study on
 755 natural and manmade global interannual fluctuations of cirrus cloud cover for the period 1984-2004, *Atmos.*
Chem. Phys., 7, 2631-2642, doi: 10.5194/acp-7-2631-2007, 2007.
- Gottelman, A., Fetzer, E. J., Eldering, A., and Irion, F. W.: The global distribution of supersaturation in the upper
 troposphere from the Atmospheric Infrared Sounder, *J. Climate*, 19, 6089-6103, doi: 10.1175/jcli3955.1, 2006.
- Gottelman, A., Hoor, P., Pan, L. L., Randel, W. J., Hegglin, M. I., and Birner, T.: The extratropical upper
 760 troposphere and lower stratosphere, *Rev. Geophys.*, 49, RG3003, doi: 10.1029/2011rg000355, 2011.
- Gottelman, A., Liu, X., Barahona, D., Lohmann, U., and Chen, C.: Climate impacts of ice nucleation, *J.*
Geophys. Res.-Atmos., 117, D20201, doi: 10.1029/2012jd017950, 2012.
- Gierens, K., Schumann, U., Helten, M., Smit, H., and Marenco, A.: A distribution law for relative humidity in
 the upper troposphere and lower stratosphere derived from three years of MOZAIC measurements, *Ann.*
 765 *Geophys.*, 17, 1218-1226, doi: 10.1007/s005850050846, 1999.
- Gierens, K., Schumann, U., Helten, M., Smit, H., and Wang, P. H.: Ice-supersaturated regions and subvisible
 cirrus in the northern midlatitude upper troposphere, *J. Geophys. Res.*, 105, 22743-22753, doi:
 10.1029/2000jd900341, 2000.
- Gierens, K., and Spichtinger, P.: On the size distribution of ice-supersaturated regions in the upper troposphere
 770 and lowermost stratosphere, *Ann. Geophys.*, 18, 499-504, doi: 10.1007/s005850050907, 2000.
- Gierens, K., and Brinkop, S.: Dynamical characteristics of ice supersaturated regions, *Atmos. Chem. Phys.*, 12,
 11933-11942, doi: 10.5194/acp-12-11933-2012, 2012.
- Gierens, K., Eleftheratos, K., and Shi, L.: Technical Note: 30 years of HIRS data of upper tropospheric humidity,
Atmos. Chem. Phys., 14, 7533-7541, doi: 10.5194/acp-14-7533-2014, 2014.
- 775 Helten, M., Smit, H. G. J., Sträter, W., Kley, D., Nédélec, P., Zöger, M., and Busen, R.: Calibration and
 performance of automatic compact instrumentation for the measurement of relative humidity from passenger
 aircraft, *J. Geophys. Res.*, 103, 25643-25652, doi: 10.1029/98jd00536, 1998.
- Helten, M., Smit, H. G. J., Kley, D., Ovarlez, J., Schlager, H., Baumann, R., Schumann, U., Nédélec, P., and
 Marenco, A.: In-flight comparison of MOZAIC and POLINAT water vapor measurements, *J. Geophys. Res.*,
 780 104, 26087-26096, doi: 10.1029/1999jd900315, 1999.
- Heysfield, A. J., Krämer, M., Luebke, A., Brown, P., Cziczo, D. J., Franklin, C., Lawson, P., Lohmann, U.,
 McFarquhar, G., Ulanowski, Z., and Tricht, K. V.: Cirrus Clouds, *Meteor. Monogr.*, 58, 2.1-2.26, doi:
 10.1175/amsmonographs-d-16-0010.1, 2017.



- Hoor, P., Gurk, C., Brunner, D., Hegglin, M. I., Wernli, H., and Fischer, H.: Seasonality and extent of
 785 extratropical TST derived from in-situ CO measurements during SPURT, *Atmos. Chem. Phys.*, 4, 1427-1442,
 doi: 10.5194/acp-4-1427-2004, 2004.
- Hoose, C., and Möhler, O.: Heterogeneous ice nucleation on atmospheric aerosols: a review of results from
 laboratory experiments, *Atmos. Chem. Phys.*, 12, 9817-9854, doi: 10.5194/acp-12-9817-2012, 2012.
- Irvine, E. A., Hoskins, B. J., and Shine, K. P.: A Lagrangian analysis of ice-supersaturated air over the North
 790 Atlantic, *J. Geophys. Res.*, 119, 90-100, doi: 10.1002/2013jd020251, 2014.
- Irvine, E. A., and Shine, K. P.: Ice supersaturation and the potential for contrail formation in a changing climate,
Earth Syst. Dynam., 6, 555-568, doi: 10.5194/esd-6-555-2015, 2015.
- Ivanova, A. R.: The tropopause: Variety of definitions and modern approaches to identification, *Russ. Meteorol.*
Hydrol., 38, 808-817, doi: 10.3103/s1068373913120029, 2013.
- 795 Jöckel, P., Tost, H., Pozzer, A., Kunze, M., Kirner, O., Brenninkmeijer, C. A. M., Brinkop, S., Cai, D. S.,
 Dyroff, C., Eckstein, J., Frank, F., Garny, H., Gottschaldt, K. D., Graf, P., Grewe, V., Kerkweg, A., Kern, B.,
 Matthes, S., Mertens, M., Meul, S., Neumaier, M., Nutz, M., Oberlander-Hayn, S., Ruhnke, R., Runde, T.,
 Sander, R., Scharffe, D., and Zahn, A.: Earth System Chemistry integrated Modelling (ESCiMo) with the
 Modular Earth Submodel System (MESSy) version 2.51, *Geosci. Model Dev.*, 9, 1153-1200, doi: 10.5194/gmd-
 800 9-1153-2016, 2016.
- Kärcher, B., and Lohmann, U.: A parameterization of cirrus cloud formation: Homogeneous freezing of
 supercooled aerosols, *J. Geophys. Res.-Atmos.*, 107, 10, doi: 10.1029/2001jd000470, 2002.
- Kärcher, B., Dörnbrack, A., and Sölch, I.: Supersaturation Variability and Cirrus Ice Crystal Size Distributions,
J. Atmos. Sci., 71, 2905-2926, doi: 10.1175/JAS-D-13-0404.1, 2014.
- 805 Kärcher, B.: Formation and radiative forcing of contrail cirrus, *Nat. Commun.*, 9, 17, doi: 10.1038/s41467-018-
 04068-0, 2018.
- Kley, D., and Stone, E. J.: Measurement of water-vapor in the stratosphere by photo-dissociation with Ly-alpha
 (1216 Å) light, *Rev. Sci. Instrum.*, 49, 691-697, doi: 10.1063/1.1135596, 1978.
- Koop, T., Luo, B. P., Tsias, A., and Peter, T.: Water activity as the determinant for homogeneous ice nucleation
 810 in aqueous solutions, *Nature*, 406, 611-614, doi: 10.1038/35020537, 2000.
- Krämer, M., Schiller, C., Afchine, A., Bauer, R., Gensch, I., Mangold, A., Schlicht, S., Spelten, N., Sitnikov, N.,
 Borrmann, S., de Reus, M., and Spichtinger, P.: Ice supersaturations and cirrus cloud crystal numbers, *Atmos.*
Chem. Phys., 9, 3505-3522, 2009.
- Krämer, M., Rolf, C., Luebke, A., Afchine, A., Spelten, N., Costa, A., Meyer, J., Zöger, M., Smith, J., Herman,
 815 R. L., Buchholz, B., Ebert, V., Baumgardner, D., Borrmann, S., Klingebiel, M., and Avallone, L.: A
 microphysics guide to cirrus clouds – Part I: Cirrus types, *Atmos. Chem. Phys.*, 16, 3463-3483, doi:
 10.5194/acp-16-3463-2016, 2016.
- Kunz, A., Schiller, C., Rohrer, F., Smit, H. G. J., Nédélec, P., and Spelten, N.: Statistical analysis of water
 vapour and ozone in the UT/LS observed during SPURT and MOZAIC, *Atmos. Chem. Phys.*, 8, 6603-6615,
 820 2008.
- Kunz, A., Mueller, R., Homonnai, V., Janosi, I. M., Hurst, D., Rap, A., Forster, P. M., Rohrer, F., Spelten, N.,
 and Riese, M.: Extending water vapor trend observations over Boulder into the tropopause region: Trend
 uncertainties and resulting radiative forcing, *J. Geophys. Res. Atmos.*, 118, 11269-11284, doi:
 10.1002/jgrd.50831, 2013.



- 825 Lamquin, N., Stubenrauch, C. J., Gierens, K., Burkhardt, U., and Smit, H.: A global climatology of upper-tropospheric ice supersaturation occurrence inferred from the Atmospheric Infrared Sounder calibrated by MOZAIC, *Atmos. Chem. Phys.*, 12, 381–405, doi: 10.5194/acp-12-381-2012, 2012.
- Lee, D. S., Pitari, G., Grewe, V., Gierens, K., Penner, J. E., Petzold, A., Prather, M. J., Schumann, U., Bais, A., Berntsen, T., Iachetti, D., Lim, L. L., and Sausen, R.: Transport impacts on atmosphere and climate: Aviation, 830 44, 4678–4734, doi: 10.1016/j.atmosenv.2009.06.005, 2010.
- Marenco, A., Thouret, V., Nédélec, P., Smit, H., Helten, M., Kley, D., Karcher, F., Simon, P., Law, K., Pyle, J., Poschmann, G., Von Wrede, R., Hume, C., and Cook, T.: Measurement of ozone and water vapor by Airbus in-service aircraft: The MOZAIC airborne program, An overview, *J. Geophys. Res.*, 103, 25631–25642, doi: 10.1029/98jd00977, 1998.
- 835 May, R. D., and Webster, C. R.: Data processing and calibration for tunable diode-laser harmonic absorption spectrometers, *J. Quant. Spectrosc. Radiat. Transfer*, 49, 335–347, doi: 10.1016/0022-4073(93)90098-3, 1993.
- Meyer, J., Rolf, C., Schiller, C., Rohs, S., Spelten, N., Afchine, A., Zöger, M., Sitnikov, N., Thornberry, T. D., Rollins, A. W., Bozóki, Z., Tátrai, D., Ebert, V., Kühnreich, B., Mackrodt, P., Möhler, O., Saathoff, H., Rosenlof, K. H., and Krämer, M.: Two decades of water vapor measurements with the FISH fluorescence 840 hygrometer: a review, *Atmos. Chem. Phys.*, 15, 8521–8538, doi: 10.5194/acp-15-8521-2015, 2015.
- Müller, R., Kunz, A., Hurst, D. F., Rolf, C., Krämer, M., and Riese, M.: The need for accurate long-term measurements of water vapor in the upper troposphere and lower stratosphere with global coverage, *Earth's Future*, 4, 25–32, doi: 10.1002/2015ef000321, 2016.
- Müller, S., Hoor, P., Berkes, F., Bozem, H., Klingebiel, M., Reutter, P., Smit, H. G. J., Wendisch, M., Spichtinger, P., and Borrmann, S.: In situ detection of stratosphere-troposphere exchange of cirrus particles in the midlatitudes, *Geophys. Res. Lett.*, 42, 949–955, doi: 10.1002/2014gl062556, 2015.
- NASA: The U.S. Standard Atmosphere, NASA, Washington, D.C., 241 pp., 1976.
- Nédélec, P., Blot, R., Boulanger, D., Athier, G., Cousin, J.-M., Gautron, B., Volz-Thomas, A., Petzold, A., and Thouret, V.: Instrumentation on commercial aircraft for monitoring the atmospheric composition on a global 850 scale : The IAGOS system, technical overview of ozone and carbon monoxide measurements, *Tellus B*, 67, doi: 10.3402/tellusb.v67.27791, 2015.
- Neis, P., Smit, H. G. J., Krämer, M., Spelten, N., and Petzold, A.: Evaluation of the MOZAIC Capacitive Hygrometer during the airborne field study CIRRUS-III, *Atmos. Meas. Tech.*, 8, 1233–1243, doi: 10.5194/amt-8-1233-2015, 2015a.
- 855 Neis, P., Smit, H. G. J., Rohs, S., Bundke, U., Krämer, M., Spelten, N., Ebert, V., Buchholz, B., Thomas, K., and Petzold, A.: Quality assessment of MOZAIC and IAGOS capacitive hygrometers: Insights from airborne field studies, *Tellus B*, 67, 28320, doi: 10.3402/tellusb.v67.28320, 2015b.
- Penner, J. E., Zhou, C., Garnier, A., and Mitchell, D. L.: Anthropogenic Aerosol Indirect Effects in Cirrus Clouds, *J. Geophys. Res.-Atmos.*, 123, 11652–11677, doi: 10.1029/2018jd029204, 2018.
- 860 Petetin, H., Jeoffrion, M., Sauvage, B., Athier, G., Blot, R., Boulanger, D., Clark, H., Cousin, J.-M., Gheusi, F., Nédélec, P., Steinbacher, M., and Thouret, V.: Representativeness of the IAGOS airborne measurements in the lower troposphere, *Elem Sci Anth.*, 6, 23, doi: 10.1525/elementa.280, 2018.
- Petzold, A., Thouret, V., Gerbig, C., Zahn, A., Brenninkmeijer, C. A. M., Gallagher, M., Hermann, M., Pontaud, M., Ziereis, H., Boulanger, D., Marshall, J., Nédélec, P., Smit, H. G. J., Frieß, U., Flaud, J.-M., Wahner, A., 865 Cammas, J.-P., Volz-Thomas, A., and IAGOS-Team: Global-Scale Atmosphere Monitoring by In-Service



- Aircraft – Current Achievements and Future Prospects of the European Research Infrastructure IAGOS, *Tellus B*, 67, 28452, doi: 10.3402/tellusb.v67.28452, 2015.
- Petzold, A., Krämer, M., Neis, P., Rolf, C., Rohs, S., Berkes, F., Smit, H. G. J., Gallagher, M., Beswick, K., Lloyd, G., Baumgardner, D., Spichtinger, P., Nedelec, P., Ebert, V., Buchholz, B., Riese, M., and Wahner, A.: Upper tropospheric water vapour and its interaction with cirrus clouds as seen from IAGOS long-term routine in situ observations, *Faraday Discuss.*, 200, 229–249, doi: 10.1039/c7fd00006e, 2017.
- Pruppacher, H. R., and Klett, J. D.: *Microphysics of Clouds and Precipitation*, 2nd ed., Kluwer Academic Publishers, AA Dordrecht, 1997.
- Reutter, P., Neis, P., Rohs, S., and Sauvage, B.: Comparison of IAGOS in-situ water vapour measurements and ECMWF ERA-Interim Reanalysis data, *Atmos. Chem. Phys. Discuss.*, 2019, 1–20, doi: 10.5194/acp-2019-573, 2019.
- Riese, M., Ploeger, F., Rap, A., Vogel, B., Konopka, P., Dameris, M., and Forster, P.: Impact of uncertainties in atmospheric mixing on simulated UTLS composition and related radiative effects, *J. Geophys. Res.-Atmos.*, 117, D16305, doi: 10.1029/2012jd017751, 2012.
- Rolf, C., Vogel, B., Hoor, P., Afchine, A., Günther, G., Krämer, M., Müller, R., Müller, S., Spelten, N., and Riese, M.: Water vapor increase in the lower stratosphere of the Northern Hemisphere due to the Asian monsoon anticyclone observed during the TACTS/ESMVal campaigns, *Atmos. Chem. Phys.*, 18, 2973–2983, doi: 10.5194/acp-18-2973-2018, 2018.
- Santee, M. L., Manney, G. L., Livesey, N. J., Schwartz, M. J., Neu, J. L., and Read, W. G.: A comprehensive overview of the climatological composition of the Asian summermonsoon anticyclone based on 10 years of Aura Microwave Limb Sounder measurements, *J. Geophys. Res.-Atmos.*, 122, 5491–5514, doi: 10.1002/2016jd026408, 2017.
- Schwartz, M. J., Read, W. G., Santee, M. L., Livesey, N. J., Froidevaux, L., Lambert, A., and Manney, G. L.: Convectively injected water vapor in the North American summer lowermost stratosphere, *Geophys. Res. Lett.*, 40, 2316–2321, doi: 10.1002/grl.50421, 2013.
- Seidel, D. J., Berger, F. H., Diamond, H. J., Dykema, J., Goodrich, D., Immeler, F., Murray, W., Peterson, T., Sisterson, D., Sommer, M., Thorne, P., Voemel, H., and Wang, J.: Reference Upper-Air Observations for Climate: Rationale, Progress, and Plans, *Bull. Am. Met. Soc.*, 90, 361–+, doi: 10.1175/2008bams2540.1, 2009.
- Sitnikov, N. M., Yushkov, V. A., Afchine, A. A., Korshunov, L. I., Astakhov, V. I., Ulanovskii, A. E., Krämer, M., Mangold, A., Schiller, C., and Ravegnani, F.: The FLASH instrument for water vapor measurements on board the high-altitude airplane, *Instrum. Exp. Tech.*, 50, 113–121, doi: 10.1134/s0020441207010174, 2007.
- Smit, H. G. J., Volz-Thomas, A., Helten, M., Paetz, W., and Kley, D.: An in-flight calibration method for near-real-time humidity measurements with the airborne MOZAIC sensor, *J. Atmos. Oceanic Technol.*, 25, 656–666, doi: 10.1175/2007jtecha975.1, 2008.
- Smit, H. G. J., Rohs, S., Neis, P., Boulanger, D., Krämer, M., Wahner, A., and Petzold, A.: Technical Note: Reanalysis of upper troposphere humidity data from the MOZAIC programme for the period 1994 to 2009, *Atmos. Chem. Phys.*, 14, 13241–13255, doi: 10.5194/acp-14-13241-2014, 2014.
- Sonntag, D.: Advances in the field of hygrometry, *Meteorol. Z.*, N.F. 3, 51–66, 1994.
- Spang, R., Gunther, G., Riese, M., Hoffmann, L., Muller, R., and Griessbach, S.: Satellite observations of cirrus clouds in the Northern Hemisphere lowermost stratosphere, *Atmos. Chem. Phys.*, 15, 927–950, doi: 10.5194/acp-15-927-2015, 2015.



- Spichtinger, P., Gierens, K., and Read, W.: The statistical distribution law of relative humidity in the global tropopause region, *Meteorol. Z.*, 11, 83-88, doi: 10.1127/0941-2948/2002/0011-0083, 2002.
- Spichtinger, P., Gierens, K., Leiterer, U., and Dier, H.: Ice supersaturation in the tropopause region over
 910 Lindenberg, Germany, *Meteorol. Z.*, 12, 143-156, doi: 10.1127/0941-2948/2003/0012-0143, 2003a.
- Spichtinger, P., Gierens, K., and Read, W.: The global distribution of ice-supersaturated regions as seen by the Microwave Limb Sounder, *Q. J. R. Meteorol. Soc.*, 129, 3391-3410, doi: 10.1256/qj.02.141, 2003b.
- Spichtinger, P., Gierens, K., and Wernli, H.: A case study on the formation and evolution of ice supersaturation in the vicinity of a warm conveyor belt's outflow region, *Atmos. Chem. Phys.*, 5, 973-987, 2005.
- 915 Spichtinger, P., and Leschner, M.: Horizontal scales of ice-supersaturated regions, 68, doi: 10.3402/tellusb.v68.29020, 2016.
- Stubenrauch, C. J., Cros, S., Guignard, A., and Lamquin, N.: A 6-year global cloud climatology from the Atmospheric InfraRed Sounder AIRS and a statistical analysis in synergy with CALIPSO and CloudSat, *Atmos. Chem. Phys.*, 10, 7197-7214, doi: 10.5194/acp-10-7197-2010, 2010.
- 920 Stubenrauch, C. J., Rossow, W. B., Kinne, S., Ackerman, S., Cesana, G., Chepfer, H., Di Girolamo, L., Getzewich, B., Guignard, A., Heidinger, A., Maddux, B. C., Menzel, W. P., Minnis, P., Pearl, C., Platnick, S., Poulsen, C., Riedi, J., Sun-Mack, S., Walther, A., Winker, D., Zeng, S., and Zhao, G.: Assessment of Global Cloud Datasets from Satellites: Project and Database Initiated by the GEWEX Radiation Panel, *Bull. Amer. Meteorol. Soc.*, 94, 1031-1049, doi: 10.1175/bams-d-12-00117.1, 2013.
- 925 Stuber, N., Forster, P., Radel, G., and Shine, K.: The importance of the diurnal and annual cycle of air traffic for contrail radiative forcing, *Nature*, 441, 864-867, doi: 10.1038/nature04877, 2006.
- Thouret, V., Cammas, J. P., Sauvage, B., Athier, G., Zbinden, R., Nédélec, P., Simon, P., and Karcher, F.: Tropopause referenced ozone climatology and inter-annual variability (1994–2003) from the MOZAIC programme, *Atmos. Chem. Phys.*, 6, 1033-1051, doi: 10.5194/acp-6-1033-2006, 2006.
- 930 WMO: Meteorology - a three-dimensional science, *WMO Bull.*, 6, 134-138, 1957.
- Zahn, A., Christner, E., van Velthoven, P. F. J., Rauthe-Schoech, A., and Brenninkmeijer, C. A. M.: Processes controlling water vapor in the upper troposphere/lowermost stratosphere: An analysis of 8 years of monthly measurements by the IAGOS-CARIBIC observatory, *J. Geophys. Res. Atmos.*, 119, 11505-11525, doi: 10.1002/2014jd021687, 2014.
- 935 Zöger, M., Afchine, A., Eicke, N., Gerhards, M. T., Klein, E., McKenna, D. S., Morschel, U., Schmidt, U., Tan, V., Tuitjer, F., Woyke, T., and Schiller, C.: Fast in situ stratospheric hygrometers: A new family of balloon-borne and airborne Lyman alpha photofragment fluorescence hygrometers, *J. Geophys. Res.*, 104, 1807-1816, doi: 10.1029/1998jd100025, 1999.